

國立臺灣大學醫學院醫療器材與醫學影像研究所

碩士論文

Graduate Institute of Medical Device and Imaging

College of Medicine

National Taiwan University

Master Thesis

利用擴散磁共振造影探討英國生物銀行 7167 名中老
年人大腦白質微結構之變化

Microstructural changes of white matter tracts across late
lifespan: A diffusion MRI study on 7167 healthy adults in
the UK Biobank

康云瀨

Yun-Jing Kang

指導教授：曾文毅 教授

Advisor: Wen-Yih Isaac Tseng, M.D., Ph.D.

中華民國 108 年 7 月

July 2019



國立臺灣大學碩士學位論文
口試委員會審定書

利用擴散磁共振造影探討英國生物銀行7167名中老年人
大腦白質微結構之變化

Microstructural changes of white matter tracts across
late lifespan: A diffusion MRI study on 7167 healthy
adults in the UK Biobank

本論文係康云瀨君（學號 R06458007）在國立臺灣大學醫
療器材與醫學影像所完成之碩士學位論文，於民國 108 年 7 月
29 日承下列考試委員審查通過及口試及格，特此證明

口試委員：

曾文毅

（簽名）

（指導教授）

黃錫

吳恩賜

系主任、所長

（簽名）

（是否須簽章依各院系所規定）

誌謝



時光荏苒，歲月如梭。回首這兩年學習與生活的點滴，所獲得到的經驗與知識，使我能滿載著收穫前往下一段旅程。在此要感謝各位師長、朋友及家人的指導與幫助。

首先要感謝我的指導教授曾文毅老師，在研究上給予我許多的幫助以及資源，在徬徨與迷惘時，引領我走到正確的方向，路途雖然陡峻漫長但一路上老師充滿細心與耐心的指導，總是能提供許多建議與啟發，使我獲益良多。感謝在 ABMRI 遇到的各位學長姐、同學與學弟妹們，有大家的相互提攜與幫助，使我在研究生活中能更加順遂，謝謝你們大家在這段日子裡帶來的歡笑與陪伴。感謝在這條路上總是在身旁相伴、相互扶持，共同成長的你們，因為有你們，為這波折起伏的人生添增了美好的色彩。此外，感謝口委老師們，在百忙之中給予我的寶貴意見，使得這論文更加的完善。

感謝這一路走來許多貴人的提點與相助，很幸運有你們，才得以完成這論文。在此，也特別感謝我最重要的家人們，因為有你們的陪伴與支持，使我能夠不顧一切的勇往直前。

最後，再次感謝在這求學生涯中所遇到的每個人，因為有你們，才能成就現在的我。謝謝你們！

"You must be the change you want to see in the world."

康云瀚 謹致於台大醫療器材與醫學影像研究所

中華民國 108 年 8 月

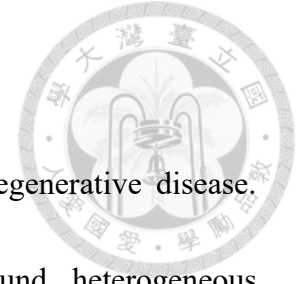
摘要



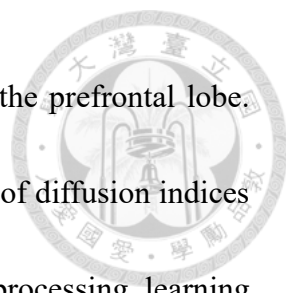
神經纖維在正常老化和神經退化性疾病中逐漸退化。過去在神經解剖學和神經影像學研究發現，不同區域的神經纖維隨著年歲增長而退化的現象具異質性；然而，仍缺乏從中年到老年完整大腦白質隨著年齡增加退化模式的完整描述。在此，我們使用英國生物銀行的擴散磁共振造影資料，來分析 7167 名 47 到 76 歲、神經系統正常的受試者老化過程神經纖維束的變化。擴散磁共振影像和結構磁共振影像資料皆在兩年內於同一台 3T 磁共振掃描儀上取得，透過四個擴散指標來看神經纖維束變化率，包含概化部分不等向性(GFA)、軸向擴散係數(AD)、徑向擴散係數(RD)、平均擴散係數(MD)，編碼 76 條神經纖維束的神經特異變化率，可呈現出神經退化的空間形態。另外我們分析 T2-FLAIR 影像與年齡相關的腦白質病變(WMHL)的變化。為了探討是否有性別差異，我們依生理性別把受試者分為男性(3368 名)與女性(3799 名)兩族群。我們的研究發現，所有受試者的神經纖維束完整性，隨年齡增長呈現緩慢穩定的下降趨勢。在大部分的慢性退行性病變的神經纖維束中(76 條中的 41 條)，隨著年齡增長，GFA 呈下降趨勢，AD、RD 和 MD 呈上升趨勢。這些纖維束包含大多數聯絡神經纖維(association fibers)、以及連接前額葉的投射神經纖維(projection fibers)和聯合神經纖維(commissure fibers)。另外有 16 條神經纖維，擴散指數隨年齡增長呈非典型變化，這些神經纖維束涉及負責快速視覺處理、學習和記憶等功能，顯示出對老化影響相對強的韌性。相較之下，WMHL 累積率最高的空間形態包括圍繞側腦室的神經纖維束，佔據周腦室和深部白質區。女性受試者的纖維完整性(GFA)退化程度較男性受試者嚴重，但在 WMHL 並沒有顯著的性別差異。這種差異表明，這兩種截然不同的年齡相關變化之間的相互作用很弱。綜合以上所述，對老化模式的完整描述可揭示衰老或抗衰老的研究，有助於找出神經退化性疾病影像的生物標記。

關鍵詞:白質老化;擴散磁共振造影;白質病變;性別差異;白質微結構特性;

Abstract



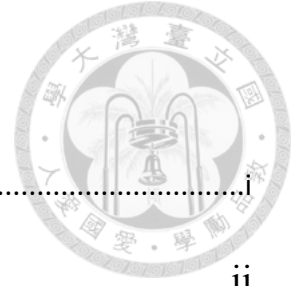
Nerve fibers degenerate during normal aging and in neurodegenerative disease. Previous neuroanatomical and neuroimaging studies have found heterogeneous vulnerabilities of nerve fibers to age-related degeneration. However, a complete description of spatial and temporal patterns of degeneration over the whole brain tracts from middle to late adulthood is lacking. Here, we analyzed diffusion MRI data in the UK Biobank and estimated tract-specific age-related changes of fiber degeneration on 7167 neurologically normal participants aged 47 to 76 years. Diffusion MRI and structure MRI were acquired on the same 3T scanner within two years. Nerve fiber degeneration was estimated in terms of the rate of change in four diffusion indices, i.e. generalized fractional anisotropy (GFA), axial diffusivity (AD), radial diffusivity (RD) and mean diffusivity (MD). Spatial patterns of fiber degeneration were rendered by encoding tract-specific rates of change to 76 fiber tracts. Age-related change of white matter hyperintensity lesions (WMHL) was also analyzed on T2-FLAIR tract wise. To appreciate sex difference, male ($N = 3368$) and female ($N = 3799$) participants were displayed separately. The results showed that the study population presented a slow and monotonic decline of fiber integrity with age. The diffusion profile of chronic degeneration change, as presented with decreased GFA, increased AD, RD and MD with age, constituted the majority of the tracts (41 out of 76 tracts). The tracts included most of the association



fibers, as well as the projection and commissure fibers connecting the prefrontal lobe. Another 16 tracts constituted a minority, exhibiting atypical changes of diffusion indices with age. These tracts involved the tracts responsible for fast visual processing, learning and memory, suggesting relative resilience to aging effects. In contrast, the spatial pattern of highest rates of WMHL accumulation comprised a cluster of tracts surrounding the lateral ventricle, occupying the periventricular and deep white matter regions. Female participants tended to have more profound degeneration of fiber integrity (GFA) than male participants, but there was no significant sex difference in WMHL. The disparity suggests weak interactions between these two distinct age-related changes. In conclusion, the complete description of degenerative patterns could shed light on the aging or anti-aging research, and facilitate the discovery of new imaging biomarkers of neurodegenerative disease.

Keywords: White matter aging; Diffusion MRI; white matter hyperintensity; Sex differences; White matter microstructural property;

Contents



口試委員審定書	i
誌謝	ii
摘要	iii
Abstract	iv
List of Figures	ix
List of Tables	x
Chapter 1 Introduction	1
1.1 Axons, connectomics, and cognitive functions	1
1.2 Degeneration of nerve fibers in brain aging	1
1.3 Patterns of fiber degeneration as a potential biomarker of abnormal brain aging.....	3
1.4 Axonal fiber tracts in neuroimaging of brain aging.....	4
1.5 Opportunities for mapping fiber degeneration in normal aging..	5
1.6 Purpose of the study	6
Chapter 2 Methods	8
2.1 Data source.....	8
2.1.1 Participants	8
2.1.2 MRI data acquisition.....	8
2.1.3 Data screening	9
2.2 Image processing.....	10
2.2.1 Reconstruction of dMRI data	10
2.2.2 Tract-based analysis of diffusion indices	11
2.2.3 Tract-specific sampling of WMHL.....	12

2.3	Correction for cerebrospinal fluid (CSF) partial volume effect	13
2.4	Tract grouping.....	14
2.5	Statistics	14
Chapter 3	Results	16
3.1	Demographics	16
3.2	Rates of change in tract integrity at different levels of tract grouping.....	17
3.3	Brain-wide patterns of rates of change in WMHL	26
3.4	Normative models of white matter tract property in the UK Biobank cohort	29
Chapter 4	Discussion	31
4.1	Summary	31
4.2	Age-related microstructural change as reflected by diffusion changes	32
4.3	White matter tracts showing a dominant diffusion change profile	34
4.4	Age-related diffusion changes deviating from the dominant profile	35
4.5	Spatial patterns of WMHL changes with age	37
4.6	Sex differences in age-related tract changes.....	38
4.7	Temporal patterns of tract changes with age.....	39
4.8	Partial volume correction for CSF	40
4.9	Limitations	41
4.10	Conclusions	42
4.11	Acknowledgments.....	43
References	44

Supplementary Files	52
SF1. Screening of MRI data.....	52
SF2. Procedures of image registration	54
SF3. The results of diffusion indices after CSF partial volume correction as compared with uncorrected diffusion indices.....	57
SF4. Detailed information of 76 tracts and 5 levels of grouping	60
SF5. Justification of the use of the linear model as opposed to the quadratic model in the analysis of age-associated change in tract integrity.....	65
SF6. The β_1 and P values of GFA, AD, RD, and MD derived from the linear model at five levels of tract grouping	67
SF7. The β_1 and P values of WMHL derived from the linear model at five levels of tract grouping	74
SF8. Normative models of white matter tract integrity of the UK Biobank cohort	76





List of Figures

Figure 1. Age distributions of male and female participants in the final analysis	6
Figure 2. The 76 tracts color-coded with β_1 values of GFA.....	19
Figure 3. The 76 tracts ranked by the magnitude of β_1 values of GFA	21
Figure 4. The 76 tracts color-coded with β_1 values of AD	22
Figure 5. The 76 tracts ranked by the magnitude of β_1 values of AD	22
Figure 6. The 76 tracts color-coded with β_1 values of RD	24
Figure 7. The 76 tracts ranked by the magnitude of β_1 values of RD	24
Figure 8. The 76 tracts color-coded with β_1 values of MD	25
Figure 9. The 76 tracts ranked by the magnitude of β_1 values of MD	25
Figure 10. The 76 tracts color-coded with β_1 values of WMHL	27
Figure 11. The 76 tracts ranked by the magnitude of β_1 values of WMHL	28
Figure SF2. The flow chart of tract-based automatic analysis (TBAA) procedures	57
Figure SF3A. Linear regression on GFA, AD, RD and MD values against V_{CSF} , before CSF partial volume correction (upper row) and after correction (lower row).....	58
Figure SF3B. Tract-mean diffusion indices overall participants, before CSF partial volume correction (upper row) and after correction (lower row)....	59
Figure SF4. Hierarchy of 5 levels of tract grouping	64
Figure SF7. The tracts that showed highest rates of WMHL increase, viewed from top (A), from side (B) and from front (C)	75
Figure SF8. Plots of means and standard deviations of the index values of each tract (i.e., GFA, AD, RD, MD, and WMHL) at each year of age	77



List of Tables

Table 1. Demographics of the participants in the full sample, imaging subsample, and final subsample	16
Table SF4. The names of the 76 tracts and the connected cortical regions .	61
Table SF6. The rate of change in GFA, AD, RD, and MD in terms of β_1 and P values, male and female participants listed separately	69
Table SF7. The rate of change in WMHL in terms of β_1 and P values, male and female participants listed separately	74
Table SF8. The mean values of GFA, AD, RD, MD, and WMHL of the whole white matter tracts at each year	76

Chapter 1 Introduction

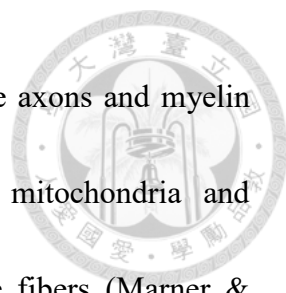


1.1 Axons, connectomics, and cognitive functions

The brain works to produce cognitive functions, and cognitive functions emerge from finely tuned signal transmission between connected neurons (Ackman, Burbridge, & Crair, 2012). Recent advance in connectomics rekindles the interest of hodology emphasizing the importance of connections between neurons for the proper functioning of cognition (Hagmann et al., 2008). Neuronal axons are physical means of interconnections of neurons and provide structural support for functional connectivity from microscopic to macroscopic levels (Sporns, Tononi, & Kotter, 2005). Mounting evidence has associated microstructural integrity of axonal fibers with cognitive functions in both normal and diseased brains (Antonenko & Floel, 2014; Wallace, Mathias, & Ward, 2018). Even in normal aging, alterations of fiber integrity with age have been found to be associated with cognitive decline (Bennett & Madden, 2014).


1.2 Degeneration of nerve fibers in brain aging

Nerve fibers change more profoundly than neurons during normal aging (Peters, Morrison, Rosene, & Hyman, 1998). Pakken-berg and Gundersen reported up to 28% reduction in white matter volume, whereas approximately 10% reduction in cortical neuron number found in humans from 20 to 90 years of age (Pakkenberg & Gundersen,



1997). Nerve fibers undergo a cascade of degenerations in both the axons and myelin sheaths. Axonal degeneration is evidenced by aggregation of mitochondria and neurofilaments, darkening of axoplasm, and overall loss of nerve fibers (Marner & Pakkenberg, 2003; Meier-Ruge, Ulrich, Bruhlmann, & Meier, 1992). Degeneration of myelin sheaths includes splitting of myelin sheaths, the formation of dense sheaths, and myelin ballooning (Bowley, Cabral, Rosene, & Peters, 2010; Peters, Moss, & Sethares, 2000). Although functionally inadequate, regeneration of the myelin sheaths occurs, forming redundant sheaths and increased number of myelin lamellae (Peters et al., 2000; Rosenbluth, Stoffel, & Schiff, 1996). Neuroanatomical studies in normal aging have noted that degeneration of fiber tracts is heterogeneous (Aboitiz, Scheibel, Fisher, & Zaidel, 1992; Liewald, Miller, Logothetis, Wagner, & Schuz, 2014; Tomasi & Volkow, 2012). Thin fibers are more vulnerable to aging effects than thick fibers, and fibers connecting the prefrontal lobe degenerate more profoundly than those connecting the posterior brain (Bartzokis, 2004). Taken together, the heterogeneity of nerve fiber degeneration may arise from different rates of degenerative change due to varied vulnerabilities of nerve fibers.

Besides age-related degeneration of axons and myelin sheaths, white matter also undergoes degeneration due to dysfunction of local cerebral blood flow (Prins & Scheltens, 2015). White matter degeneration induced by dys-regulated blood flow has



been found associated with small vessel disease (Munoz Maniega et al., 2017) and has a characteristic signal change known as white matter hyperintensity lesions (WMHL) on magnetic resonance imaging (MRI) using a T2-weighted fluid-attenuated imaging sequence (T2-FLAIR) (O'Sullivan et al., 2002; Wong et al., 2019). Like nerve fiber degeneration, many studies have shown that WMHL also increases with age, and is associated with cognitive decline (Brugulat-Serrat et al., 2019). However, the relationship between age-related changes in WMHL and nerve fiber integrity remains unclear.

1.3 Patterns of fiber degeneration as a potential biomarker of abnormal brain aging

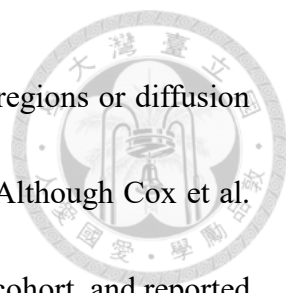
Nerve fiber degeneration may have occurred at least one decade before overt symptoms of cognitive decline (Araque Caballero et al., 2018). If there is brain pathology, the fiber alterations associated with it will present on top of the alterations due to normal aging (Seltzer et al., 2004). Therefore, differentiating pathological alterations from alterations due to normal aging requires an accurate description of the alteration patterns in normal aging. By comparing with the patterns of tract alteration due to normal aging, we can detect the tracts deviating from the normal reference patterns. Furthermore, different neurodegenerative diseases may have different patterns of deviant tracts early in

the course of the disease and might serve as a biomarker of risk prediction or therapeutic monitoring.



1.4 Axonal fiber tracts in neuroimaging of brain aging

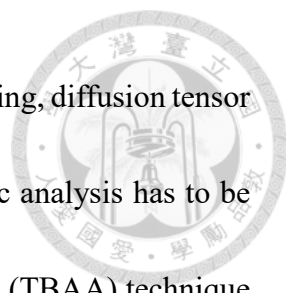
Diffusion MRI (dMRI) is the only noninvasive imaging modality that can probe nerve fiber integrity in vivo (Beaulieu, 2002). The diffusion signal measured by dMRI is sensitive to the geometric property of underlying microstructure. Diffusion tensor imaging (DTI) is a widely used dMRI technique which models the diffusion phenomenon as a 3D Gaussian function of displacement probability (Basser, Mattiello, & LeBihan, 1994). By fitting the Gaussian function as a rank-2 tensor, scalar indices can be extracted to capture different features of diffusivity of the probed microstructure. To date, the most commonly used diffusion indices include axial diffusivity (AD), radial diffusivity (RD), mean diffusivity (MD) and fractional anisotropy (FA). Axial diffusivity refers to the first eigenvalue corresponding to the first eigenvector of the diffusion tensor, and RD refers to the mean of the second and third eigenvalues. Mean diffusivity can determine by averaging the three eigenvalues of the diffusion tensor, and FA is calculated to indicate the degree of anisotropy of the diffusion tensor. Many studies have used DTI to demonstrate alterations of fiber integrity in normally aged brains or those afflicted by neurodegenerative diseases (Gold & Keller, 2012). However, most studies have been



conducted in small sample sizes or focusing on limited numbers of regions or diffusion indices, limiting generalization of the results (Chen-Plotkin, 2014). Although Cox et al. analyzed brain MRI of 3513 generally people from the UK Biobank cohort, and reported some age-associated features of brain structures (Cox et al., 2016), they did not specifically examine the rate of change in fiber degeneration across whole brain in normal aging. To have a brain-wide view of fiber degeneration in normal aging, it is imperative to build a reference of tract- and sex-specific trajectories of the four common diffusion indices in a large cohort of late adulthood.

1.5 Opportunities for mapping fiber degeneration in normal aging

The dMRI data archived in the UK Biobank provide us an opportunity to build normal aging patterns of fiber degeneration. UK Biobank prospectively gathers extensive health-related data in a cohort of 500,000 participants, including questionnaires, physical and cognitive measures, and biological samples (Miller et al., 2016). Participants were in their 5th to 8th decade of age at baseline recruitment. In 2016, an imaging extension was initiated to scan 100,000 adults from the existing cohort; each scanned once at dedicated imaging centers. The first imaging center built in Cheadle, Greater Manchester, England, to establish feasibility and scanned 10,000 subjects over a two-year ramp-up period. To convert dMRI raw data to tract-specific information about tract integrity in such a huge

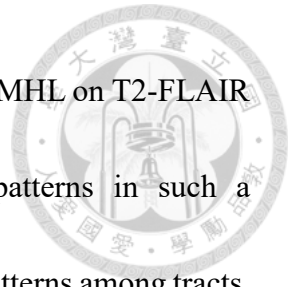


amount of data is challenging. An automatic pipeline from data screening, diffusion tensor reconstruction, quality assurance, image registration, to tract-specific analysis has to be set up. Recently, we have developed a tract-based automatic analysis (TBAA) technique and established a complete processing pipeline for dMRI data (Chen et al., 2015). To date, the TBAA technique and processing pipeline have been applied to clinical studies in various neurological or psychiatric diseases (Chen et al., 2018; Chien, Chen, Hsu, Tseng, & Gau, 2017; Huang et al., 2018; Lo et al., 2019; Tsai et al., 2019; Wu et al., 2015). Taking the advantage of large dMRI data provided by the UK Biobank and our automatic analysis pipeline, we are ready to build a comprehensive pattern of nerve fiber degeneration in a healthy cohort from 47 to 76 years.

1.6 Purpose of the study

Therefore, the purpose of the study was to build a reference pattern of fiber degeneration in normal aging, providing comprehensive information for each fiber tract, in each diffusion index, and for each sex. To appreciate the heterogeneity of fiber degeneration, we described the degeneration patterns at different levels of fiber tract grouping, from the whole brain, three fiber systems, down to the individual fiber tracts. To gain insight into the microstructural alterations in fiber degeneration, we expressed the degeneration patterns in terms of rates of change in four diffusion indices, i.e., GFA, AD,

RD, and MD. In the same manner, we also analyzed the change of WMHL on T2-FLAIR images for comparison. By describing the fiber degeneration patterns in such a comprehensive way, we aimed to identify the differences in change patterns among tracts, between male and female participants, and between diffusion indices and WMHL. The knowledge gained in this study could shed light on white matter aging and potentially facilitate the discovery of imaging biomarkers of neurodegenerative disease.



Chapter 2 Methods

2.1 Data source


2.1.1 Participants

The total population of the recruited participants up to September 2017 consisted of 238720 male and 263908 female participants (Sudlow et al., 2015). Approximately 2% of the participants received MRI scanning, and among them, 8830 people had usable MRI data of T1-weighted (T1w), T2-FLAIR, and dMRI. See Supplementary File 1 for details of unusable MRI data

2.1.2 MRI data acquisition

MRI scanning was performed on 3T Siemens Skyra System running VD13A SP4 operating system, with a 32-channel RF receive head coil. T1-weighted images were acquired using a 3D magnetization-prepared rapid gradient-echo pulse sequence: Inversion time (TI) / repetition time (TR) = 880/2000 ms, Field-of-view (FOV) = 208 x 256 x 256 mm³, resolution = 1 x 1 x 1 mm³, sagittal plane, and in-plane acceleration factor = 2. T2-FLAIR images were acquired using 3D SPACE with fat saturation: TI / TR = 1800 / 5000 ms, FOV = 192 x 256 x 256 mm³, resolution = 1.05 x 1 x 1 mm³, sagittal plane, and in-plane acceleration factor = 2. Diffusion MRI utilized a twice-refocused spin-echo echo-planar imaging sequence with 10 baseline images ($b = 0 \text{ s mm}^{-2}$), 50 diffusion-





weighted images with $b = 1,000 \text{ s mm}^{-2}$ and 50 images with $b = 2,000 \text{ s mm}^{-2}$; imaging parameters: TR/TE = 3600/92 ms, FOV = $104 \times 104 \text{ mm}^2$, in-plane resolution = $2 \times 2 \text{ mm}^2$, slice thickness = 2 mm, slice number = 72, trans-axial plane, and multislice acceleration = 3. In addition to the primary dMRI data, 3 $b = 0$ images with reversed-phase encoding acquired for later field map estimation along with 3 $b = 0$ images with standard phase encoding. The estimated field map used for distortion correction in the dMRI datasets.

2.1.3 Data screening

To ensure that participants at scanning were neurologically healthy, the participants who had past history of neurological or psychiatric disease, substance abuse, malignancy as listed in Supplementary File 1, or an IQ out with the range 100 ± 30 (mean ± 2 SD) were excluded from the analysis. We further excluded image data with poor image quality, including poor SNR, incomplete image data, failed distortion correction, or large intra-scanning displacement between dMRI and T1w image. There were 7692 people passed the data screening, including 3653 male and 4039 female participants.

2.2 Image processing

2.2.1 Reconstruction of dMRI data

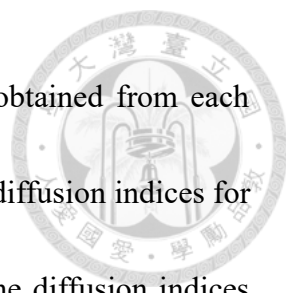


We used MAP-MRI algorithm to calculate diffusion indices for each individual (Ozarslan et al., 2013). The MAP-MRI algorithm describes the MR signals in q-space in terms of a linear combination of Hermite functions (Avram et al., 2016), which form an orthonormal and complete basis, to approximate diffusion signal profiles. MAP-MRI is an extension of DTI because Hermite functions of zero-order are precisely a Gaussian function. In contrast, the higher-order terms, which are the orthogonal corrections to the Gaussian approximation, account for the non-Gaussian components of the diffusion signals. Besides, the Fourier transforms of Hermite functions are also Hermite functions. As a result, the diffusion propagator and orientation distribution function could be readily reconstructed from the coefficients estimated by fitting the diffusion signals with Hermite functions. From the orientation distribution function, we calculated generalized fractional anisotropy (GFA)(Tuch, 2004), which is analogous to FA in DTI. Mean MD, RD, and AD calculated as those defined in the DTI model. These indices have regarded as surrogate markers indicating different aspects of the microstructural property of white matter (Alexander et al., 2011).

2.2.2 Tract-based analysis of diffusion indices



To perform diffusion index sampling along each of the fiber tracts, tract-based automatic analysis was conducted to sample the diffusion indices from 76 predefined major fiber tract bundles over the whole brain (Chen et al., 2015). The 76 major fiber tract bundles were previously reconstructed in a DSI template (Hsu, Lo, Chen, Wedeen, & Isaac Tseng, 2015), NTU-DSI-122 which was constructed in the ICBM-152 space, using deterministic streamline-based tractography with multiple regions of interest defined in the automated anatomical labeling atlas (Lyttelton, Boucher, Robbins, & Evans, 2007). To register dMRI data of UK Biobank, a DTI template, NTU-DSI-122-DTI, was built from NTU-DSI-122 by fitting the diffusion signals with the tensor model. After the registration process, the coordinates of the 76 tracts were transformed from NTU-DSI-122-DTI to the individual native space with corresponding deformation maps. The deformation maps were obtained through a group-wise registration, which included anatomical information provided by the T1-weighted images and microstructural information provided by the diffusion datasets. Detailed procedures of the two-step registration are described in Supplementary File 2. Each fiber tract bundle was equally divided into 100 steps, and the values of diffusion indices were sampled in native space along the step coordinates. The output of tract-based analysis for each participant was a 2D array of the sampled diffusion indices (x-axis: 100 steps along sampling coordinates; y-axis: 76 white matter tract



bundles). Consequently, four 2D arrays of diffusion indices were obtained from each participant corresponding to GFA, AD, RD, and MD. Tract-specific diffusion indices for each tract were calculated by calculating the arithmetic means of the diffusion indices over 100 steps. Data analysis was conducted using the Maxwell High Performance Computing Cluster of the University of Aberdeen IT Service (www.abdn.ac.uk/staffnet/research/hpc.php), provided by Dell Inc. and supported by Alces Software consisting of 800 CPU cores and a total memory size of 12 TB.

2.2.3 Tract-specific sampling of WMHL

The percentage of WMHL was estimated on T2-FLAIR using the lesion segmentation tool at each voxel (Schmidt et al., 2012). This step rigidly registered T2-FLAIR image to T1w image. Given the deformation maps from NTU-DSI-122-DTI to individual DTI datasets, and to native T2-FLAIR images, WMH lesions were sampled along each of neural fiber tracts and produced a 100-by-76 2D array of WMHL in terms of the probability of WMHL at each step of tract sampling coordinates. The mean WMHL value for each tract was calculated by calculating the geometric means of $(1 - \text{probability})$ over 100 steps and subtracted by 1.

2.3 Correction for cerebrospinal fluid (CSF) partial volume effect

Given the deformation maps from NTU-DSI-122-DTI to individual DTI datasets, and to T1w images, TPM of CSF was sampled along each of neural tracts and produced a 100-by-76 2D array of CSF probability corresponding to the volume fraction of CSF (V_{CSF}) at each step along each fiber tract. The information was used to correct for the partial volume effect of CSF in the tract-specific sampling of diffusion indices. The sampled diffusion index value at each step of the tract is the apparent diffusion index (D_{app}) which is the sum of the volume fraction of white matter (V_{WM}) times the diffusion index of white matter (D_{WM}) and V_{CSF} times the diffusion index of CSF (D_{CSF}), i.e. $D_{\text{app}} = V_{\text{WM}} \times D_{\text{WM}} + V_{\text{CSF}} \times D_{\text{CSF}} = (1 - V_{\text{CSF}}) \times D_{\text{WM}} + V_{\text{CSF}} \times D_{\text{CSF}} = D_{\text{WM}} + (D_{\text{CSF}} - D_{\text{WM}}) \times V_{\text{CSF}}$. Given the measured D_{app} and V_{CSF} at each step, the diffusion index without CSF partial volume effect D_{WM} can be obtained by regressing D_{app} values against V_{CSF} : $D_{\text{app}} = \beta_0 + \beta_1 \times V_{\text{CSF}}$, where β_0 was equivalent to D_{WM} , and β_1 was equivalent to $D_{\text{CSF}} - D_{\text{WM}}$. Having obtained β_1 from the regression model, the corrected value of the diffusion index, i.e., D_{WM} or β_0 , was calculated by subtracting the term $\beta_1 \times V_{\text{CSF}}$ from D_{app} in a stepwise manner. The regression was performed on each individual using 100-by-76 apparent diffusion indices and 100-by-76 CSF probabilities. The regression model provided β_1 values for us to calculate corrected diffusion index at each step of the tract. The results of

diffusion indices after CSF partial volume correction as compared with uncorrected diffusion indices are detailed in Supplementary File 3.

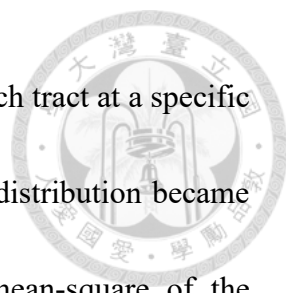


2.4 Tract grouping

To appreciate the rate of change in tract property from the whole brain to tract-wise levels, 76 tracts were grouped into 5 levels of subdivisions, namely 76 tracts, 25 tract groups, ten subsystems, three fiber systems, and the whole brain. Detailed information of 76 tracts and grouping can be found in Supplementary File 4. To provide normative models of tract-specific indices of the current cohort, the mean and standard deviation for each tract were calculated over the population at each year and in each gender.

2.5 Statistics

To determine the rate of change in each diffusion index with age, a linear regression model $Y = \beta_0 + \beta_1 \times \text{age}$ was used, where Y indicated each individual's mean diffusion index value for each tract entity at 5 different levels of tract grouping. Male and female participants were analyzed separately. The rationale of using the linear regression model was based on the fact that after 45 years of age the diffusion indices change almost linearly with age. The use of the linear model in contrast to the quadratic model was justified in Supplementary File 5.



Unlike diffusion indices, the geometric means of WMHL for each tract at a specific year resembled a one-sided distribution with the peak at zero. The distribution became wider as the age increased. Therefore, we calculated the root-mean-square of the geometric means of the tract to represent the mean WMHL of the population each year. The root-mean-square values across 30 years of the specific tract were then used to fit the linear regression model. Linear regression model was applied to each tract (total number of sample $m = 76$), each tract group ($m = 25$), each subsystem ($m = 10$), each fiber system ($m = 3$), and the whole brain ($m = 1$). The Bonferroni correction conducted for multiple comparisons within each level of grouping. To appreciate the spatial location of tract entities encoded with different rates of change, the values of β_1 that passed the statistical test were rendered in tables and figures.

Chapter 3 Results

3.1 Demographics

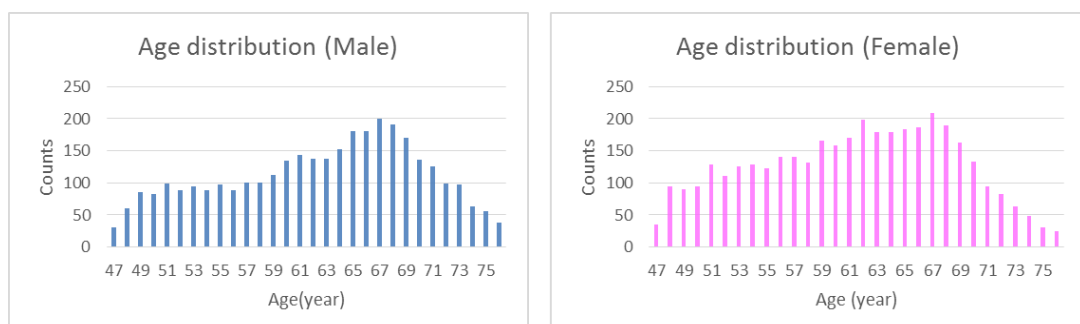


To ensure the quality of DTI data, we excluded participants whose MRI data had either one of the GFA, AD, RD, and MD falling outside the range of mean \pm 4 SD in any one of the 76 tracts. After quality assurance, 7167 participants (93.2% of 7692 people) were included in the final analysis, including 3368 male and 3799 female participants with age ranging from 47 to 76 years. Table 1 lists the demographics of the recruited participants, and Figure 1 shows the age distributions of male and female participants in the final analysis.

Table 1. Demographics of the participants in the full sample, imaging subsample, and final subsample.

Variable	Full Sample		Imaging subsample		Final subsample	
Sex	Male	Female	Male	Female	Male	Female
N	238720	263908	3653	4039	3368	3799
Percentage	47.5%	52.5%	47.5%	52.5%	47.0%	53.0%
Age, Mean (<i>SD</i>) years	61.47 (7.06)	61.47 (7.20)	61.99 (8.78)	61.99 (8.78)	61.02 (7.13)	61.74 (7.10)
IQ, Mean (<i>SD</i>)	101.4 (15.41)	98.84 (14.54)	99.55 (3.80)	101.2 (3.63)	100.55 (12.96)	100.71 (12.87)

Figure 1. Age distributions of male and female participants in the final analysis.



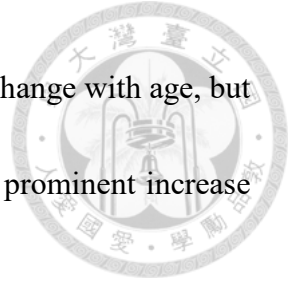
3.2 Rates of change in tract integrity at different levels of tract grouping



Rates of change (i.e., β_1) and P values of GFA, AD, RD, and MD at five levels of tract grouping are described and listed in Supplementary File 6. We identified a predominant global change of diffusion indices at the whole-brain level, but the changes deviating from the global change started to emerge when we went down to more fine-grained levels. When we categorized the tracts according to shared profiles of change in diffusion indices, we found four main groups exhibiting distinct profiles among the 76 tracts. The first group constituted the majority of tracts (41 tracts out of 76 tracts) showing increased AD and RD with age, accompanied by increased MD and decreased GFA. The first group included most of the association fibers, as well as most of the projection and commissure fibers connecting the prefrontal lobe. The second group comprised the tracts (8 tracts) exhibiting an age-related increase in AD, variable changes in RD, accompanied by increased MD and GFA with age. The second group included bilateral corticospinal tracts of hand (CST_Hand), thalamic radiations to the precentral cortex (TR_Precentral) and postcentral cortex (TR_Postcentral), callosal fibers connecting the superior temporal lobe (CF_Sup Temp), and posterior commissure (PC). The third group had the tracts (4 tracts) presenting an age-related increase in AD and decrease in RD, accompanied by increased GFA and varied changes in MD. The tracts included right CST of toe

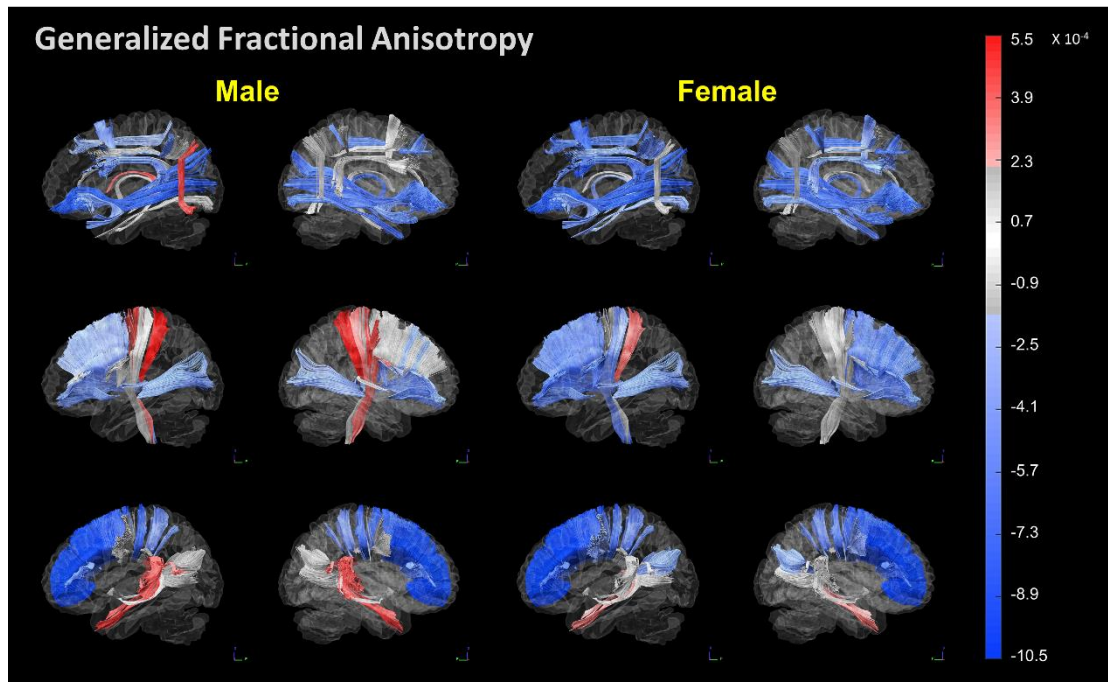
(CST_Toe), and callosal fibers connecting the middle temporal lobe (CF_Mid temp), the temporal pole (CF_Temp pole), and hippocampus (CF_Hippo). The fourth group comprised the tracts (4 tracts) exhibiting an age-related decrease in AD and RD, accompanied by decreased MD and varied changes in GFA. The tracts in the fourth group included bilateral thalamic radiations to the visual cortex (TR_Opt, i.e., optic tracts), left perpendicular fasciculus (PF), and callosal fibers connecting the ventrolateral prefrontal cortex (CF_VLPFC).

Figure 2 shows the 76 tracts color-coded with the β_1 value in GFA, male and female participants rendered separately. GFA generally decreased with age in both male and female participants as presented by predominantly blue hue on the tracts. However, some tracts showed increased GFA with age, opposite to the global trend of GFA decline. In the association fibers, most of the tracts showed decreased GFA with age; only stria terminalis (ST) and PF showed increased GFA with age. The commissure fibers exhibited a gradient of GFA decrease, from the anterior brain (most prominent decline in the prefrontal lobe) to the posterior brain (least decline in the parietal and occipital lobes). In contrast, the commissure fibers connecting the temporal lobe demonstrated increased GFA with age. In the projection fibers, the frontostriatal tracts and thalamic radiations connecting the prefrontal lobe and visual cortex demonstrated GFA decline with age, whereas CST and thalamic radiations connecting the somatosensory cortex showed increased GFA with age.



Both male and female participants showed a similar pattern of GFA change with age, but female participants tended to have more prominent decline but less prominent increase than did male participants.

Figure 2. The 76 tracts color-coded with the rate of change in GFA. Red hue indicates tracts with significant increase with age, blue hue indicates tracts with significant decrease with age, and gray hue indicates tracts without a significant rate of change. Association (upper row), projection (middle row), and commissure (lower row) fibers are rendered in male (left) and female (right) participants separately. To visualize the rate of change, the magnitude of β_1 value was rescaled by amplification of 10^4 .






Figure 3 shows the 76 tracts ranked by the magnitude of β_1 values of GFA, male and female placed side-by-side for the ease of viewing. We can see that male participant had more tracts with significant positive β_1 values, whereas female participants had more tracts with significant negative β_1 values. Moreover, male participants presented significant positive β_1 values with the magnitude larger than female participants. In contrast, female participants had significant negative β_1 values with the magnitude generally larger than did male participants. Out of 76 tracts, male participants had 31 tracts (41%) with significant negative β_1 values, whereas female participants had 51 tracts (67%). The results indicate that female participants have significantly more aggravated age-associated decline of tract integrity than male participants ($\chi^2 = 10.59, p = 0.001$).

Figure 3. The 76 tracts ranked by the magnitude of their rates of change (β_1) in GFA. Red hue indicates significant positive β_1 values, blue hue indicates significant negative β_1 values, and gray hue indicates β_1 values without statistical significance. To visualize the rate of change, the magnitude of β_1 values was rescaled by amplification of 10^4 .

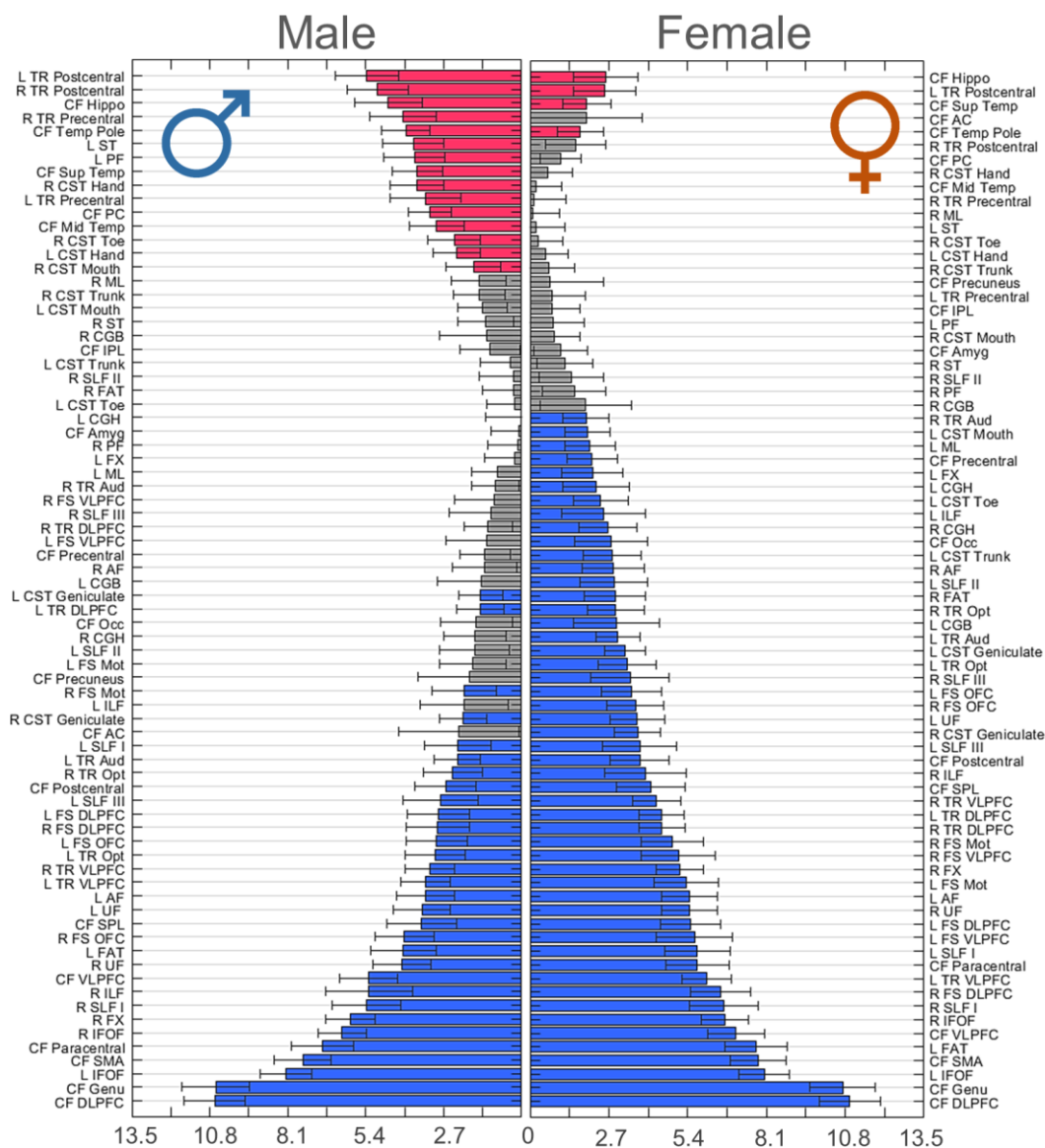


Figure 4 shows the 76 tracts color-coded with the β_1 value in AD, and Figure 5 shows the 76 tracts ranked by the magnitude of β_1 values of AD. There was a predominant trend of AD increase with age, and the projection fibers connecting the frontal lobe exhibited the most prominent increase. A few tracts showed significantly decreased AD with age, these tracts were distributed in association fibers (left ST, left PF), projection fibers (left CST_Toe, left medial lemniscus ML, bilateral TR_Opt) and commissure fibers (CF_VLPFC and CF_Temp pole).

Figure 4. The 76 tracts color-coded with β_1 values of AD. To visualize the rate of change, the magnitude of β_1 value was rescaled by amplification of 10^4 .

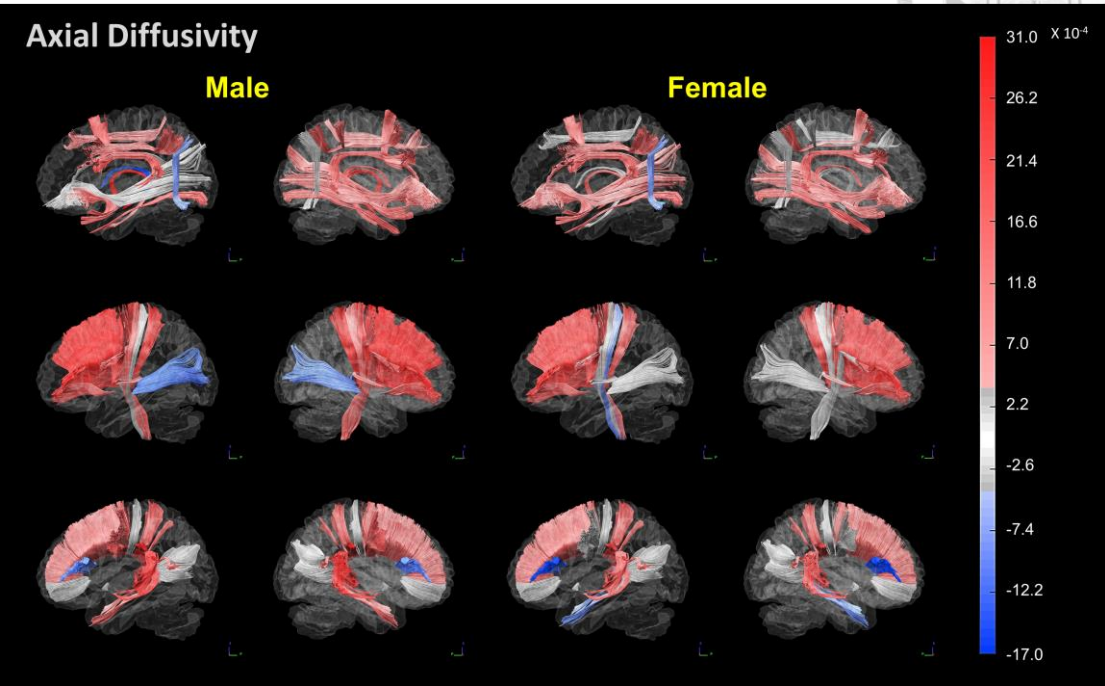
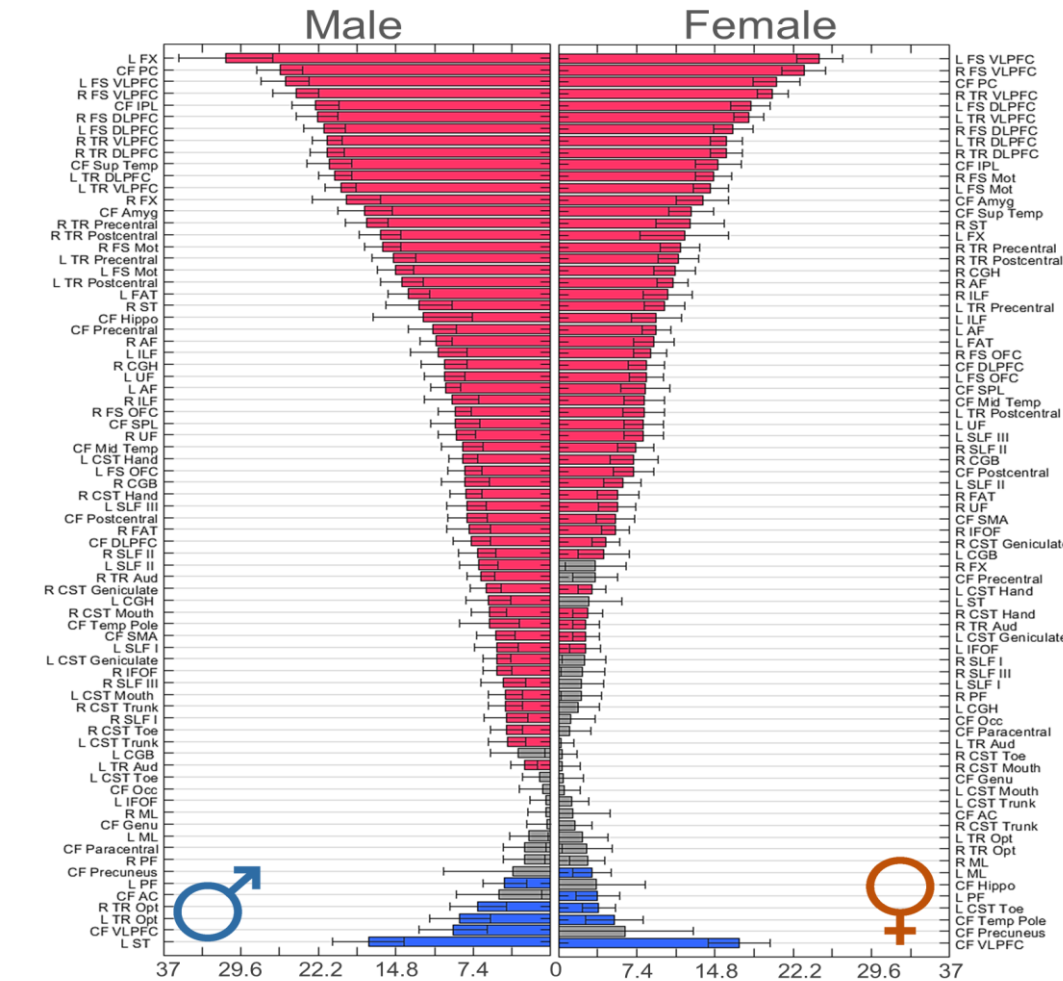


Figure 5. The 76 tracts ranked by the magnitude of β_1 values of AD.



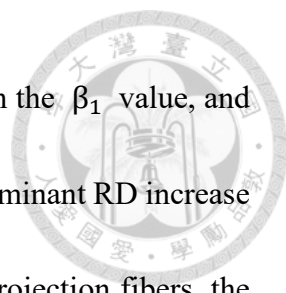


Figure 6 and 7 show, respectively, the 76 tracts color-coded with the β_1 value, and those ranked by the magnitude of β_1 values of RD. There was predominant RD increase with age, but unlike AD which was most prominent in the frontal projection fibers, the increase was presented in most of the association fibers, and most of the projection and commissure fibers connecting the frontal lobe. There were also a few tracts showing significant decrease with age, most prevalent in the callosal fibers (CF_VLPFC, CF_Precentral, CF_Precuneus, CF_Occ, and all callosal fibers connecting the temporal lobe), followed by the projection fibers (CST_Hand, CST_Trunk and CST_Toe, and bilateral TR_Opt), and least in the association fibers (bilateral PF).

Figure 8 and 9 show, respectively, the 76 tracts color-coded with the β_1 value, and those ranked by the magnitude of β_1 values of MD. There was predominant MD increase with age, and the pattern was similar to that of RD; the tracts involved most of the association fibers and most of the projection and commissure fibers connecting the frontal lobe. The tracts that presented significant decrease with age had a pattern similar to AD, involving the association fibers (left ST, bilateral PF), projection fibers (left CST_Toe, right CST_Trunk, right ML, bilateral TR_Opt) and commissure fibers (CF_VLPFC, CF_precuneus and CF_Temp pole).

Figure 6. The 76 tracts color-coded with β_1 values of RD. To visualize the rate of change, the magnitude of β_1 value was rescaled by amplification of 10^4 .

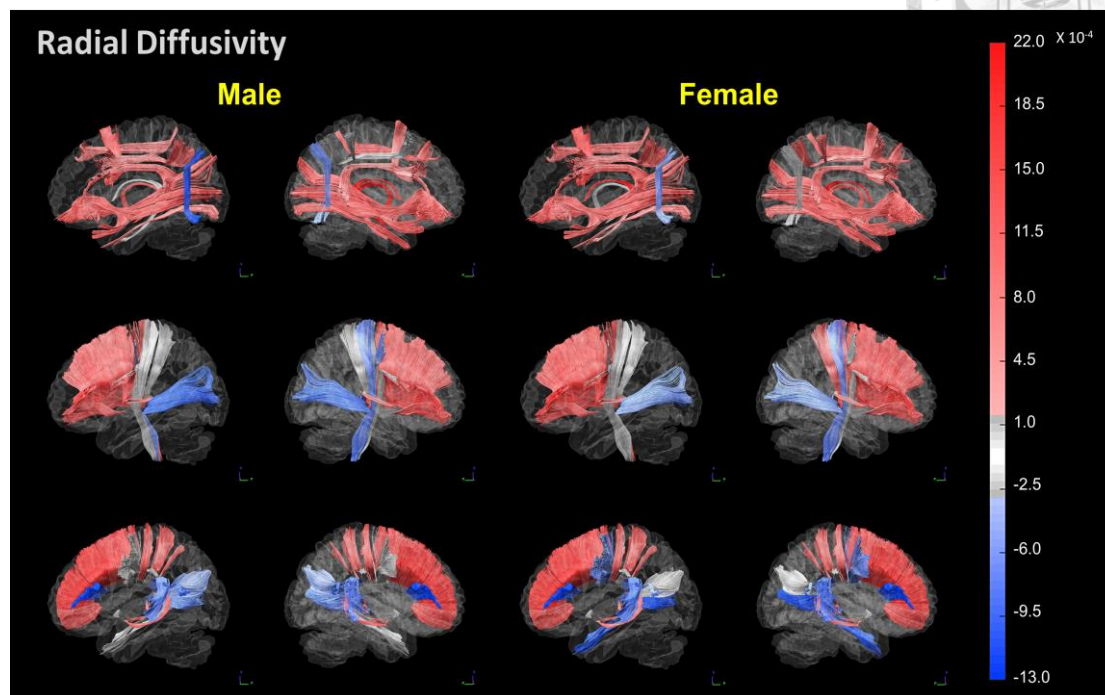


Figure 7. The 76 tracts ranked by the magnitude of β_1 values of RD

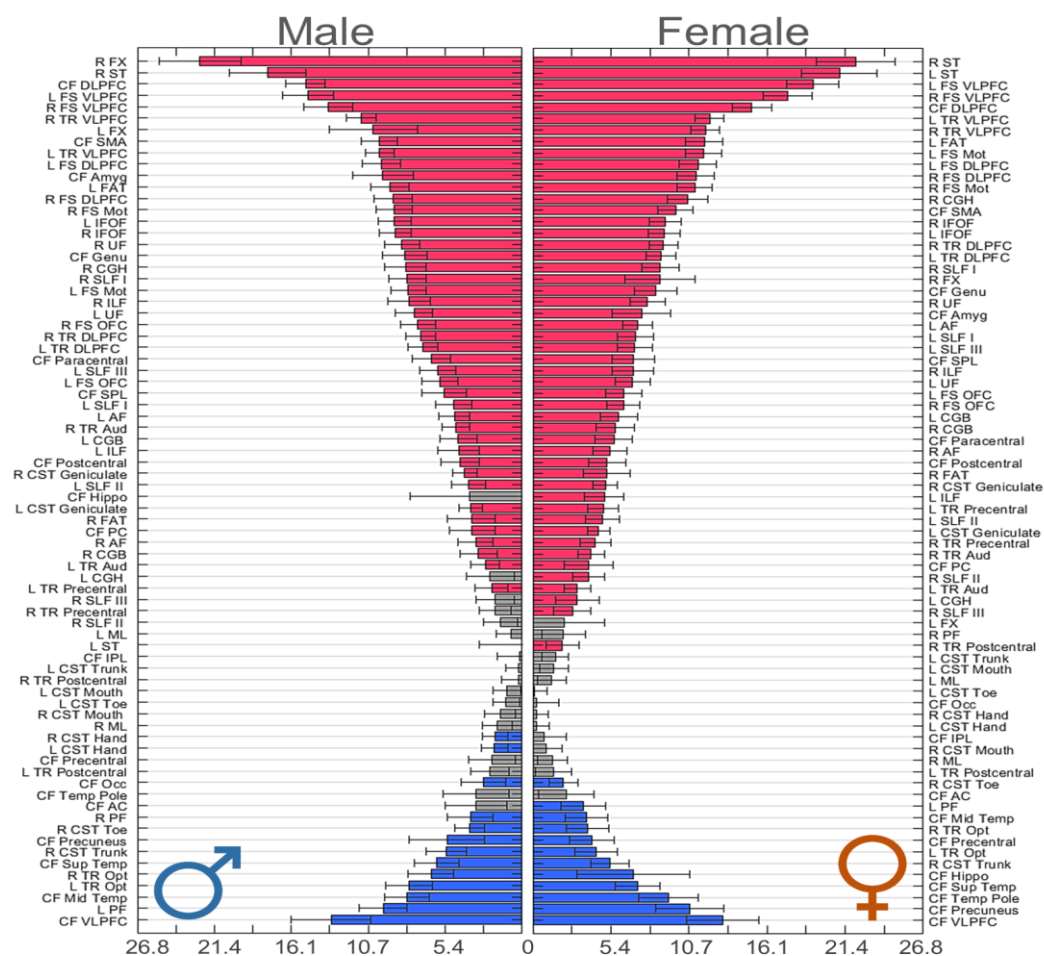


Figure 8. The 76 tracts color-coded with β_1 values of MD .To visualize the rate of change, the magnitude of β_1 value was rescaled by amplification of 10^4 .

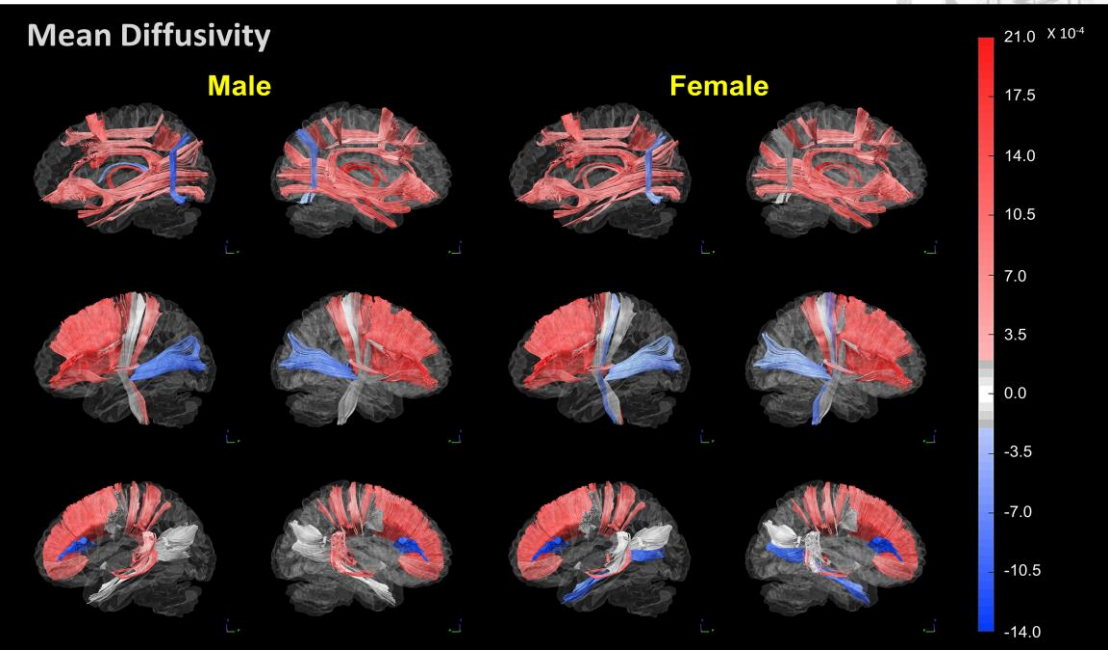
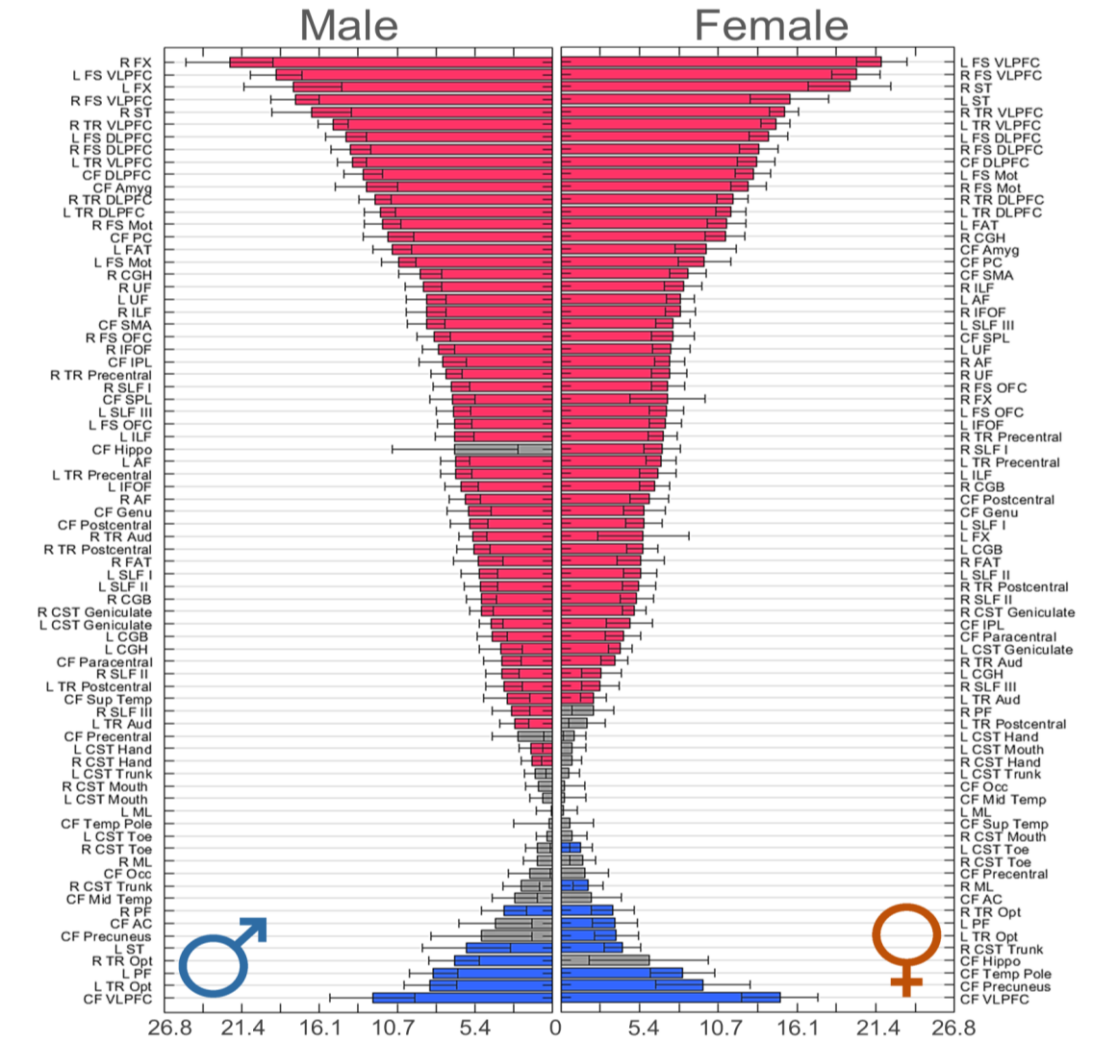


Figure 9. The 76 tracts ranked by the magnitude of β_1 values of MD



3.3 Brain-wide patterns of rates of change in WMHL

Figure 10 shows the 76 tracts color-coded with the rate of change (i.e. β_1 value) in WMHL, male and female participants rendered separately. In both sexes, the callosal and projection fibers tended to have more frequent involvement than the association fibers. The tracts with significantly high rates of change in WMHL formed a cluster of tracts surrounding the lateral ventricles (see Figure SF7), corresponding to the typical locations of WMHL in the periventricular and deep white matter regions. This cluster included nine callosal fiber tracts, I.e. CF_Genu, CF_DLPFC, CF_VLPFC, CF_SMA, CF_Precentral, CF_Precuneus, CF_Occ, CF_Mid temp and CF_Hippo, eight projection fiber tracts, i.e. right CST_Geniculate, left TR_DLPFC, bilateral FS_VLPFC, TR_VLPFC, and TR_Opt, and two association fibers, i.e. bilateral IFOF. Besides higher rates of WMHL change, this cluster of 19 tracts also showed a significantly larger mean WMHL load than the rest of 57 tracts. Supplementary File 7 provides a detailed list of the β_1 and P values of WMHL at five levels of tract grouping, as well as the tractogram the 19 tracts and their mean WMHL values as compared with the rest of the tracts.

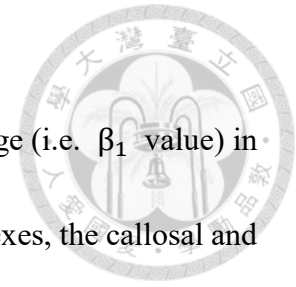


Figure 10. The 76 tracts color-coded with the rate of change (i.e., β_1) in WMHL. Red hue indicates tracts with significant increase with age, blue hue indicates tracts with significant decrease with age, and gray hue indicates tracts without significant rate of change. Association (upper row), projection (middle row), and commissure (lower row) fibers are rendered in male (left) and female (right) participants separately. To visualize the rate of change, the magnitude of β_1 value was rescaled by amplification of 10^3 , plus one, and natural logarithm transform.

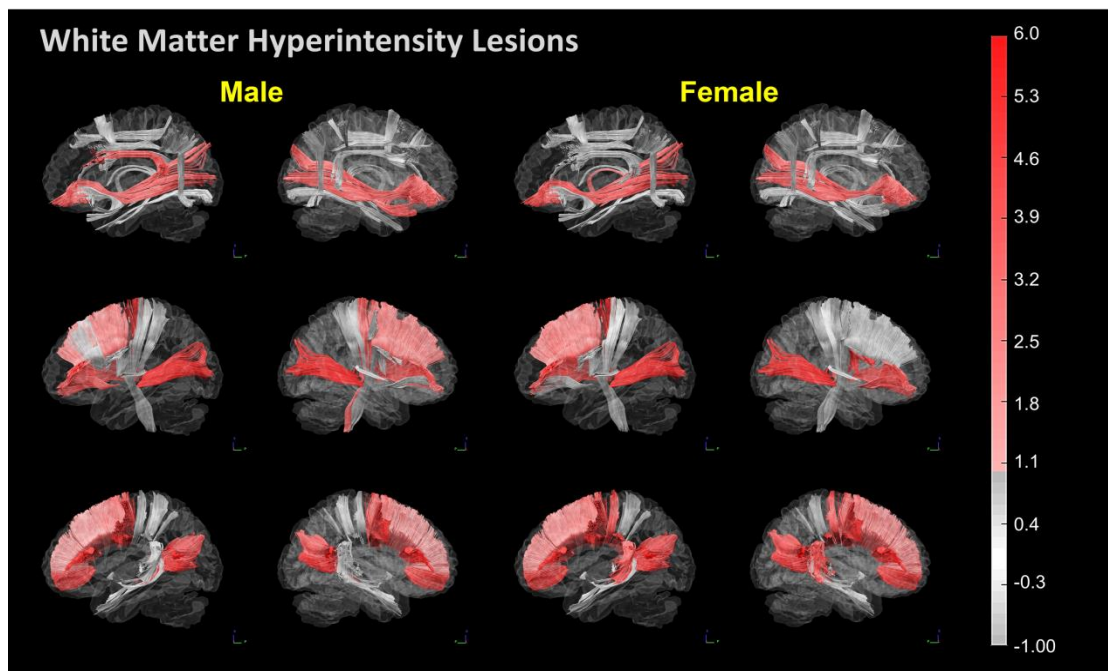
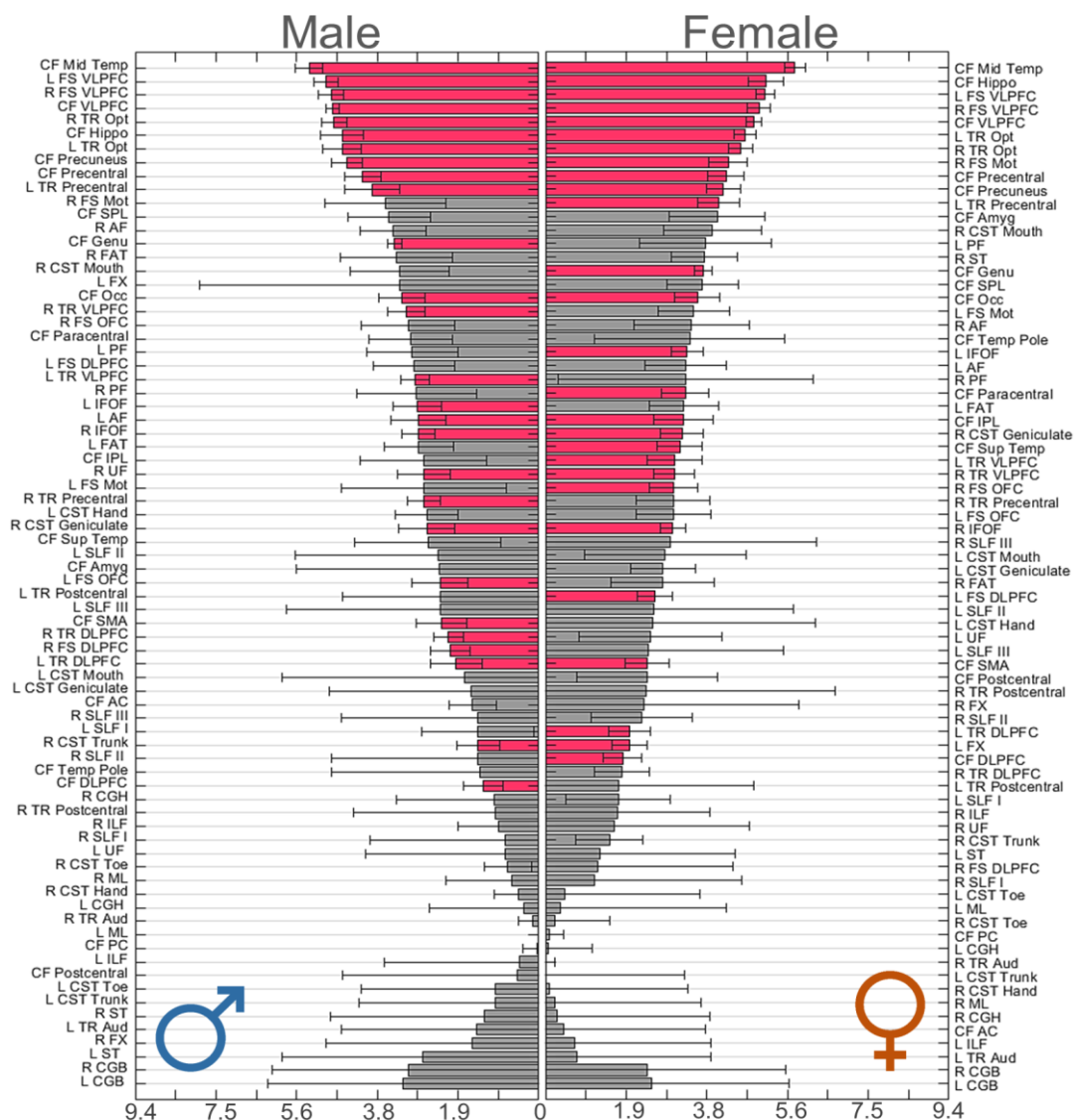


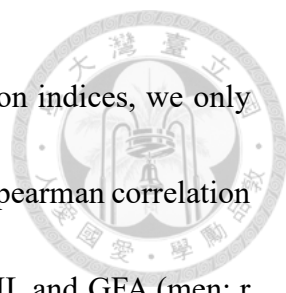
Figure 11 shows the 76 tracts ranked by the magnitude of β_1 values of WHML, male and female placed side-by-side for the ease of viewing. Both male and female participants had the same number of tracts with significant rates of increase in WHML (27 out of 76 tracts, 35.5%; $\chi^2 = 0$, $p = 1$). Moreover, the top ten tracts showing the highest rates of WHML increase had striking similarity between sexes; nine out of ten were shared by

male and female participants. These tracts included CF_VLPFC, CF_Precentral, CF_Precuneus, CF_Mid Temp, CF_Hippo, bilateral TR_Opt, and bilateral FS_VLPFC.

Figure 11. The 76 tracts ranked by the magnitude of their rate of change in WMHL (β_1)

values. Red hue indicates significant positive β_1 values, blue hue indicates significant negative β_1 values, and gray due indicates β_1 values without statistical significance. To visualize the rate of change, the magnitude of β_1 values was rescaled by amplification of 10^3 , plus one, and natural logarithm transform.



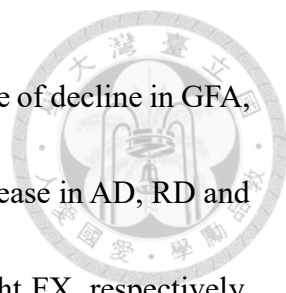


To examine the associations between WMHL values and diffusion indices, we only used tract-specific mean WMHL values that were greater than zero. Spearman correlation coefficients showed significant but weak correlations between WMHL and GFA (men: $r = -0.059$; $p = 0.001$, and women: $r = -0.088$; $p = 0.000$), AD (men: $r = 0.215$; $p = 0.000$, and women: $r = 0.205$; $p = 0.000$), RD (men: $r = 0.114$; $p = 0.000$, and women: $r = 0.129$; $p = 0.000$) and MD (men: $r = 0.165$; $p = 0.000$, and women: $r = 0.168$; $p = 0.000$).

3.4 Normative models of white matter tract property in the UK

Biobank cohort

The mean values of GFA, AD, RD, MD, and WMHL of the whole white matter tracts at each year were calculated and listed in Supplementary File 8. Normality test was performed for each tract at each year and sex. In a total of 18240 tests (i.e., 4 indices x 76 tracts x 30 years x 2 sexes = 18240), only 30 tests did not pass the test. Therefore, means and standard deviations of diffusion indices (including GFA, AD, RD, and MD) were determined for each of the 76 tracts, and at each year, male and female participants presented separately. From the mean value of the population at 47 years old and the β_1 value, the total change across 30 years was calculated for each index at each tract and each sex. We observed that the change of tract integrity from 47 to 76 years old was very small. The total change across 30 years was at most 13% concerning the initial tract



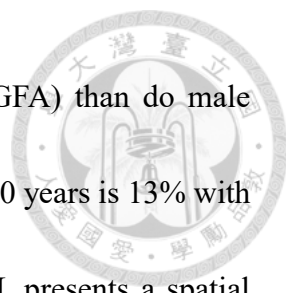
integrity at 47 years old. For male, the CF_DLPFC had the highest rate of decline in GFA, and the total change over 30 years was -6%. The highest rates of increase in AD, RD and MD were found in posterior commissure (CF_PC), right FX and right FX, respectively, with the total changes being 8%, 13% and 9%. For female, the CF_DLPFC exhibited the highest rate of decline in GFA, and the total change over 30 years was -6%. The highest rates of increase in AD, RD and MD were found in left FS_VLPFC, right ST, and left FS_VLPF, and the total changes were 8%, 13% and 10%, respectively. The largest accumulated WMHL over 30 years was found in CF_Mid temp, with the mean probabilities of 0.2535 and 0.2121 for male and female participants, respectively.

Chapter 4 Discussion

4.1 Summary



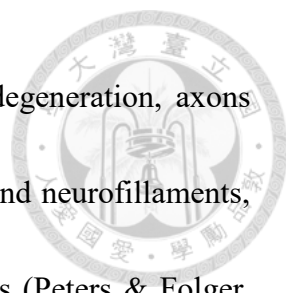
This study analyzed the largest cohort of neurologically healthy participants in the world and provided a comprehensive description of age-related changes in nerve fiber tracts in late adulthood encompassing whole brain tracts and a complete array of white matter properties. We identified subtle but statistically robust changes in normal aging and delineated characteristic spatial and temporal patterns. The results of the present study are valuable because the MRI data are acquired by the same MRI scanner and analyzed by the same analysis software, avoiding the variability across different scanners or different analysis techniques. The main findings are summarized as follow. 1) There is a dominant age-related decline in tract integrity occupying 54% of the tracts (41 out of 76 tracts), presenting a diffusion profile of decreased GFA, and increased AD, RD and MD with age. This profile involves most of the association fibers, and the commissure fibers and projection fibers connecting the prefrontal lobe. 2) In addition to the dominant profile of tract integrity change, there are three atypical profiles occupying 21% of the tracts (16 out of 76 tracts). The first profile presented increased AD, varied RD, increased MD and increased GFA with age, the second profile exhibited increase AD, decreased RD, increased GFA and varied MD with age, and the third showed decrease AD, decreased RD, decreased MD and varied GFA with age. 3) Female participants tend to have more



tracts with the significant age-related decrease of tract integrity (GFA) than do male participants. The largest amount of change in diffusion indices over 30 years is 13% with respect to the amount at 47 years. 4) Age-related change in WMHL presents a spatial pattern very different from those for diffusion indices. The tracts that show prominent rates of increase in WMHL surround the lateral ventricles, corresponding to the typical locations of WMHL in the periventricular and deep white matter regions. The rates of change in WMHL vary drastically among tracts, but male and female patients exhibit similar degrees of involvement. The unique spatial and temporal patterns of fiber degeneration may correspond to what has been found in neurobiology and may shed light on the mechanism of normal brain aging.

4.2 Age-related microstructural change as reflected by diffusion changes

Changes of white matter microstructure during normal aging have been extensively studied using light microscopy or electron microscopy in humans and rhesus monkeys (Aboitiz et al., 1992; Bowley et al., 2010; Liewald et al., 2014; Pakkenberg et al., 2003; Peters & Sethares, 2002; Tomasi & Volkow, 2012). The knowledge of microstructural changes during aging and responsive changes in diffusion indices can guide proper interpretation of our results. The main age-related change in white matter microstructure

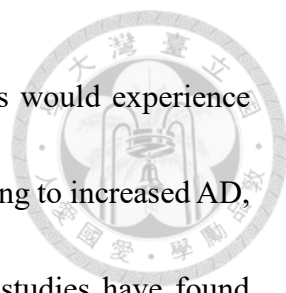


entails degenerations of axons and myelin sheaths. During axon degeneration, axons undergo a series of changes from the aggregation of mitochondria and neurofilaments, darkening of axoplasm, and leading to complete loss of axon fibers (Peters & Folger, 2013). Myelin sheath degeneration entails splitting of laminated sheaths, the formation of dense sheaths, myelin ballooning, redundant sheaths and increased number of myelin lamellae (Peters & Folger, 2013). It is also reckoned that thin fibers are more susceptible to age-related degeneration than thick fibers and that the proportions of thin fibers with respect to thick fibers vary across different tracts (Aboitiz et al., 1992; Liewald et al., 2014; Tomasi & Volkow, 2012). These microstructural changes can be probed non-invasively using dMRI because the diffusion measurement time of approximately 50 msec allows water molecules to travel approximately 15 microns (Le Bihan & Iima, 2015). Therefore, the measured diffusion indices represent the ensemble average of microstructural features within the range of 15 microns. Although diffusion indices do not specifically correspond to microscopic features, many studies have reported changes in diffusion indices in response to microstructural alterations (Beaulieu, 2002). For instance, microstructural alterations in axons are associated with AD changes (Budde, Xie, Cross, & Song, 2009), whereas alterations in myelin sheaths are associated with RD changes (Jelescu et al., 2016; Song et al., 2002). MD represents the overall mobility of water molecules in the microstructure, and it increases in the chronic stage of fiber

degeneration (Concha, Gross, Wheatley, & Beaulieu, 2006). GFA represents the strength of anisotropic diffusion in the microstructure, and its variation depends on the relative changes in AD and RD. Given the changes of individual diffusion indices in response to microstructural changes and partial interdependence among indices, it is necessary to take the complete profile of the diffusion indices into consideration to gain insight into the underlying microstructural changes.

4.3 White matter tracts showing a dominant diffusion change profile

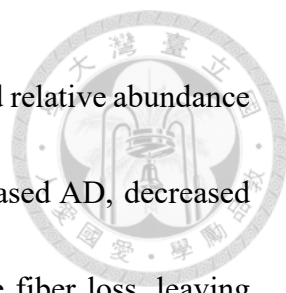
The dominant age-related diffusion change profile, i.e. increased AD, RD, MD and decreased GFA with age, implies a chronic stage of fiber degeneration (Fig. 2 and Table SF6). We found that the tracts with this unique profile involve most of the association fibers, and the commissure fibers and projection fibers of the prefrontal lobe. This spatial pattern is consistent with neurobiological studies reporting the presence of abundant thin fibers in association fibers (Liewald et al., 2014), prefrontal commissure fibers (Aboitiz et al., 1992) and prefrontal projection fibers (Tomasi & Volkow, 2012). Thin fibers have thinner myelin sheaths, mature later in life and are more vulnerable to age-related degeneration than thick fibers. The white matter tracts possessing abundant thin fibers would undergo more profound fiber loss together with axon and myelin sheath alterations in the remaining fibers, leading to reduced fiber density and increased extracellular space.



As a result, water molecules diffusing in these white matter regions would experience higher mobility parallel and orthogonal to the axonal directions, leading to increased AD, RD and MD, and decreased GFA with age. In fact, previous DTI studies have found selective age-related decline in the association fibers (Hugenschmidt et al., 2008; Stadlbauer, Salomonowitz, Strunk, Hammen, & Ganslandt, 2008), prefrontal projection fibers (Jang & Seo, 2015), and prefrontal commissure fibers (Sullivan, Adalsteinsson, & Pfefferbaum, 2006; Yoon, Shim, Lee, Shon, & Yang, 2008).

4.4 Age-related diffusion changes deviating from the dominant profile

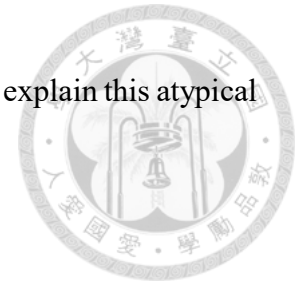
Compared with the dominant diffusion profile, three atypical profiles might represent milder stages of age-related degeneration of white matter microstructure (Fig. 2 and Table SF6). The profile of increased AD, varied RD, increased MD, and increased GFA with age might represent axons with the existence of fiber loss (increased AD) and a mixture of myelin sheath alterations from dense sheaths, increased myelin lamellae, myelin ballooning and redundant sheaths (varied RD). Dense sheath and increased myelin lamellae may lead to reduced RD, whereas myelin ballooning and redundant sheaths may cause increased RD. The resulting increase or decrease in RD would depend on relative frequencies of myelin changes contributing to two opposite diffusion changes. In the same vein, the profile of increased AD, decreased RD, increased GFA, and varied MD with age



might represent axons in the presence of fiber loss (increased AD) and relative abundance of dense or increased sheaths (decreased RD). The profile of decreased AD, decreased RD, decreased MD, and varied GFA with age might represent little fiber loss, leaving organelle accumulation (decreased AD) and abundant dense sheaths (decreased RD) as the early alterations of white matter microstructure.

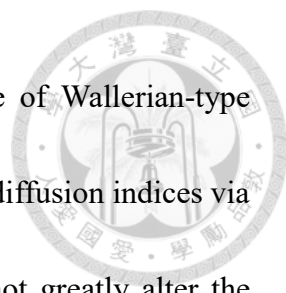
Interestingly, we found that these atypical profiles are located in the tracts related to the motor and somatosensory functions (CST_Toe, CST_Hand, and thalamic radiations connecting the precentral and postcentral cortices), and visual functions (TR_Opt, perpendicular fasciculus, CF_PC). These tracts are known to contain relatively abundant thick axons for fast processing speed, and thick axons are known to be less vulnerable to the aging effect than thin axons (Bartzokis, 2004). Another group of tracts with atypical profiles mainly involves callosal fibers connecting the temporal lobe, and CF_VLPFC. Because callosal fibers connecting the temporal lobe (including CF_Sup temp, CF_Mid temp, CF_Temp pole, and CF_Hippo) directly or indirectly connected to the hippocampus where neural stem cells reside to support learning and memory. Experimental observations suggest that the relative mild alteration of the hippocampus might be attributed to axonal plasticity against age-related degeneration (Decker, 1987; Mora & Phil, 2013). As for CF_VLPFC, although it belongs to the callosal fibers connecting the prefrontal lobe, it exhibits a completely opposite diffusion change profile compared to

other callosal fibers of the prefrontal lobe. Further study is required to explain this atypical finding.



4.5 Spatial patterns of WMHL changes with age

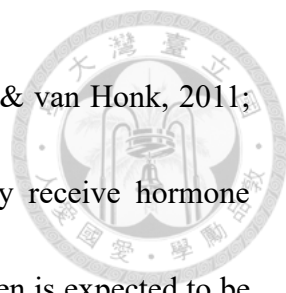
The spatial patterns of the tracts with the highest rates of WMHL increase constitute a cluster of tracts occupying the periventricular and deep white matter regions. This pattern is very different from the spatial pattern of the age-related change in diffusion indices; it is predominantly located in the prefrontal regions. The disparity of the spatial patterns between WMHL and diffusion indices can be explained by different vulnerabilities of the white matter regions subjected to different pathogenic causes. WMHL is thought to arise from impaired autoregulation of local cerebral blood flow due to aging penetrating arterioles, leading to accumulation of WMHL in the downstream regions (O'Sullivan et al., 2002) (i.e. periventricular and deep white matter regions). Recent studies also propose dysfunction of the blood-brain barrier of the arterioles as another contributing factor to the formation of WMHL (Wong et al., 2019). In contrast, the change in diffusion indices is mainly due to age-related degeneration of the axons and myelin sheaths. The vulnerability depends on the constituents of the fiber tracts, i.e., the volume fraction of the thin fibers, rather than the proximity of WMHL regions. Reginold et al. found that the diffusion indices were altered in tracts traversing WMHL regions



more severely than the remote tracts, and suggested the presence of Wallerian-type degeneration (Reginold et al., 2018). Although WMHL might affect diffusion indices via secondary degeneration, our results indicate that this effect does not greatly alter the general pattern of age-related degeneration of nerve fibers. The weak associations between WMHL and diffusion indices ($r^2 < 0.03$) also suggest that age-related changes in WMHL and fiber integrity are two independent processes with different pathogenic causes which have very the interactions.

4.6 Sex differences in age-related tract changes


This study found that female participants present more tracts with the significant age-related decrease of tract integrity (GFA) than do male participants. The sex difference in age-related change of tract integrity has been reported previously and is considered to be partially related to the menopausal effect. Since the age of participants in this study ranged from 47 to 76 years, the majority of female participants had experienced premenopause, perimenopause, and postmenopause stages. Estrogen is known to have potent neuroprotective effects, and reduced estrogen concentration in female-specific endocrine transitions has been found to be associated with white matter degeneration, enhanced AD-related pathologies in the brain, cognitive decline and neurodegenerative disease in elderly women (Berent-Spillson et al., 2012; Ha, Xu, & Janowsky, 2007;



Mosconi et al., 2017; Peper, van den Heuvel, Mandl, Hulshoff Pol, & van Honk, 2011; Ycaza Herrera & Mather, 2015). Although some participants may receive hormone therapy, the effect is inconsistent and the number of medicated women is expected to be too low to balance the overall reduction of estrogen in the population. However, our speculation should be validated by further controlling factors such as education, occupation, lifestyle, and cardiovascular risks between male and female participants because these factors may also have detrimental effects on white matter integrity (Tian et al., 2015; Williamson et al., 2018).

4.7 Temporal patterns of tract changes with age

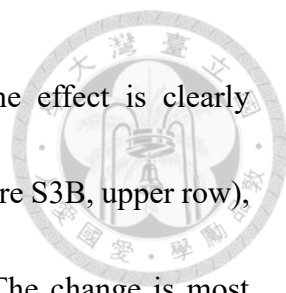
One of the contributions of this study is to provide comprehensive normative values of tract integrity obtained from the largest healthy population in the world from 47 to 76 years of age (Supplementary File 8). These normative values can be used to convert an individual's tract-specific index to age- and sex-specific Z scores. The converted Z scores can then serve as a reference to screen aberrant tract integrity in the incoming participants of the UK Biobank. With this normative data, we are able to clarify the total amount of tract-specific change over the span of 30 years in late adult life. In diffusion indices, the amount of change is not larger than 13% over 30 years, or 0.43% per year, relative to the initial index values at 47 years old. The magnitude of the change is comparable to Lebel's



fitted results on a lifespan cohort interpreted in the same age range (Lebel et al., 2012), and Ritchie's longitudinal results on a cohort scanned at 73 and 76 years old (Ritchie et al., 2017). Amlien et al. conducted a longitudinal study on patients with mild cognitive impairment and found a greater rate of decline in white matter integrity compared to healthy people (Amlien et al., 2013). Using this normative data as a tract-specific rate of change in normal aging, we could detect accelerated degeneration of specific tracts in pathological brain aging. For instance, a longitudinal study on a group of participants who were mutation carriers of early-onset autosomal-dominant Alzheimer's disease showed a change of 0.27% per year in the IFOF and genu of the corpus callosum (Araque Caballero et al., 2018), exceeding the estimated change rates of 0.13% and 0.08%, respectively, in our healthy population.

4.8 Partial volume correction for CSF

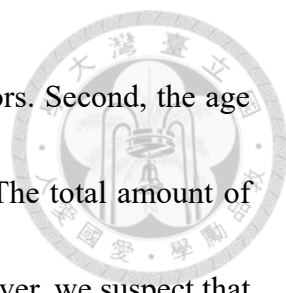
Partial volume effect is one of the major technical concerns in tract-specific analysis, especially in tracts that are surrounded by or adjacent to the CSF space (Ritchie et al., 2018; Waiter et al., 2019). The voxels contaminated by CSF can cause erroneous estimate of diffusion indices. To correct for the partial volume effect, we leverage the information about CSF volume fraction from the tissue probability map and use a linear model to determine the value of β_1 (equivalent to $D_{\text{CSF}} - D_{\text{WM}}$, see Methods, CSF partial volume



effect correction) (Kao, Hsu, & Tseng, 2019). The partial volume effect is clearly observed in the 2D arrays of diffusion indices before correction (Figure S3B, upper row), and largely diminished after correction (Figure S3B, upper row). The change is most obvious in bilateral fornices, bilateral stria terminalis, and the callosal fibers connecting the temporal lobes, presenting overly decreased GFA and increased AD, RD and MD before correction. The 2D arrays also reveal that the partial volume effect increases with age. If not corrected, this age-related effect would lead to overestimation of the rate of decline. Indeed, our previous analysis without CSF partial volume correction demonstrated age-related GFA decline in bilateral stria terminalis, and the callosal fibers connecting the hippocampus and temporal pole (Waiter et al., 2019), and they turned to GFA increase after correction. Only bilateral fornices, which showed age-related decline before correction, still exhibited a significant decline after correction.

4.9 Limitations

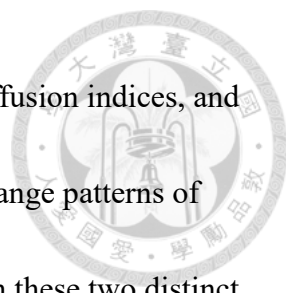
The study has limitations that caution the implication of the results. First, the study found that female participants had a more prominent age-related change in tract integrity than male participants. The study did not include comprehensive demographic data to control for possible confounders such as education, occupation, lifestyle, and cardiovascular risks. We cannot ascertain whether the difference purely arises from the



sex difference or it is confounded by other medical or lifestyle factors. Second, the age range of the participants in this study ranged from 47 to 76 years. The total amount of change over this age range was quite small, only 13% at most. However, we suspect that the rate of change in tract integrity will accelerate after 76 years old. In addition, some tracts showed increased tract integrity with age. It is interesting to know whether the integrity of these tracts might have been slowly increasing since childhood or there is an inflection point in the middle age. These questions can only be answered by studying a cohort with the age range older or younger than that of the present study.

4.10 Conclusions

Age-related change of white matter tract degeneration has been analyzed in 7167 neurologically healthy participants aged 47 to 76 years. Spatial and temporal patterns of change in diffusion indices and WMHL have been characterized in male and female participants. Diffusion indices present a dominant change pattern implicating chronic degeneration of axons and myelin sheaths. However, there are atypical change patterns of diffusion indices in tracts responsible for fast visual processing, learning, and memory, suggesting relative resilience to aging effects. Female participants exhibit more profound degenerative change than male participants, presumably due in part to female-specific menopausal effects. The



changing pattern of WMHL is very different from that of the diffusion indices, and it shows no significant sex difference. The disparity between change patterns of diffusion indices and WMHL suggests weak interaction between these two distinct age-related changes. The normative degenerative patterns provided by this study could shed light on aging or anti-aging research, and facilitate the discovery of new imaging biomarkers for detecting neurodegenerative disease.

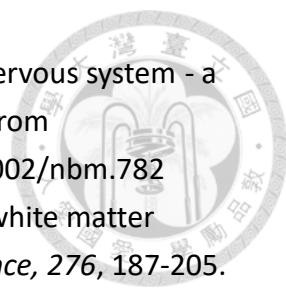
4.11 Acknowledgments


This research was approved by the UK Biobank (application number: 24089) and was supported by the Roland Sutton Academic Trust (grant number: 0039/R/16). We would like to acknowledge the valuable contributions of members of the UK Biobank Imaging Working Group and the UK Biobank coordinating centre. UK Biobank (including the imaging enhancement) has supported by the UK Medical Research Council and the Wellcome Trust. We are grateful for the provision of simultaneous multi-slice (multiband) pulse sequence and reconstruction algorithms from the Center for Magnetic Resonance Research, University of Minnesota. Finally, we are extremely grateful to all UK Biobank study participants, who have generously donated their time to make this resource possible.

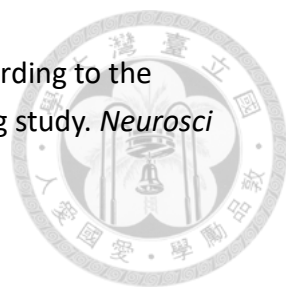



References

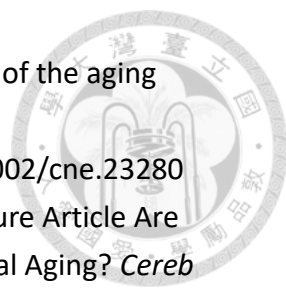
- Aboitiz, F., Scheibel, A. B., Fisher, R. S., & Zaidel, E. (1992). Fiber composition of the human corpus callosum. *Brain Res*, 598, 143-153.
- Ackman, J. B., Burbridge, T. J., & Crair, M. C. (2012). Retinal waves coordinate patterned activity throughout the developing visual system. *Nature*, 490(7419), 219-225. Retrieved from <https://www.ncbi.nlm.nih.gov/pubmed/23060192>. doi:10.1038/nature11529
- Alexander, A. L., Hurley, S. A., Samsonov, A. A., Adluru, N., Hosseinbor, A. P., Mossahebi, P., . . . Field, A. S. (2011). Characterization of cerebral white matter properties using quantitative magnetic resonance imaging stains. *Brain Connect*, 1(6), 423-446. doi:10.1089/brain.2011.0071
- Alfaro-Almagro, F., Jenkinson, M., Bangerter, N. K., Andersson, J. L. R., Griffanti, L., Douaud, G., . . . Smith, S. M. (2018). Image processing and Quality Control for the first 10,000 brain imaging datasets from UK Biobank. *Neuroimage*, 166, 400-424. doi:10.1016/j.neuroimage.2017.10.034
- Amlien, I., Fjell, A. M., Walhovd, K. B., Selnes, P., Stenset, V., Grambaite, R., . . . Fladby, T. (2013). Mild Cognitive Impairment: Cerebrospinal Fluid Tau Biomarker Pathologic Levels and Longitudinal Changes in White Matter Integrity. *Radiology*, 266, 295-303.
- Antonenko, D., & Floel, A. (2014). Healthy aging by staying selectively connected: a mini-review. *Gerontology*, 60(1), 3-9. Retrieved from <https://www.ncbi.nlm.nih.gov/pubmed/24080587>. doi:10.1159/000354376
- Araque Caballero, M. A., Suarez-Calvet, M., Duering, M., Franzmeier, N., Benzinger, T., Fagan, A. M., . . . Ewers, M. (2018). White matter diffusion alterations precede symptom onset in autosomal dominant Alzheimer's disease. *Brain*, 141(10), 3065-3080. Retrieved from <https://www.ncbi.nlm.nih.gov/pubmed/30239611>. doi:10.1093/brain/awy229
- Avram, A. V., Sarlls, J. E., Barnett, A. S., Ozarslan, E., Thomas, C., Irfanoglu, M. O., . . . Bassar, P. J. (2016). Clinical feasibility of using mean apparent propagator (MAP) MRI to characterize brain tissue microstructure. *Neuroimage*, 127, 422-434. doi:10.1016/j.neuroimage.2015.11.027
- Bartzokis, G. (2004). Age-related myelin breakdown: a developmental model of cognitive decline and Alzheimer's disease. *Neurobiol Aging*, 25(1), 5-18. doi:10.1016/j.neurobiolaging.2003.03.001
- Basser, P. J., Mattiello, J., & LeBihan, D. (1994). MR Diffusion Tensor Spectroscopy and Imaging. *Biophysical Journal*, 66, 259-267.

- 
- Beaulieu, C. (2002). The basis of anisotropic water diffusion in the nervous system - a technical review. *NMR Biomed*, 15(7-8), 435-455. Retrieved from <https://www.ncbi.nlm.nih.gov/pubmed/12489094>. doi:10.1002/nbm.782
- Bennett, I. J., & Madden, D. J. (2014). Disconnected aging: cerebral white matter integrity and age-related differences in cognition. *Neuroscience*, 276, 187-205. Retrieved from <http://www.ncbi.nlm.nih.gov/pubmed/24280637>. doi:10.1016/j.neuroscience.2013.11.026
- Berent-Spillion, A., Persad, C. C., Love, T., Sowers, M., Randolph, J. F., Zubieta, J. K., & Smith, Y. R. (2012). Hormonal environment affects cognition independent of age during the menopause transition. *J Clin Endocrinol Metab*, 97(9), E1686-1694. Retrieved from <https://www.ncbi.nlm.nih.gov/pubmed/22730514>. doi:10.1210/jc.2012-1365
- Bowley, M. P., Cabral, H., Rosene, D. L., & Peters, A. (2010). Age changes in myelinated nerve fibers of the cingulate bundle and corpus callosum in the rhesus monkey. *J Comp Neurol*, 518(15), 3046-3064. Retrieved from <http://www.ncbi.nlm.nih.gov/pubmed/20533359>. doi:10.1002/cne.22379
- Brugulat-Serrat, A., Salvado, G., Sudre, C. H., Grau-Rivera, O., Suarez-Calvet, M., Falcon, C., . . . Study, A. (2019). Patterns of white matter hyperintensities associated with cognition in middle-aged cognitively healthy individuals. *Brain Imaging Behav*. Retrieved from <https://www.ncbi.nlm.nih.gov/pubmed/31278650>. doi:10.1007/s11682-019-00151-2
- Budde, M. D., Xie, M., Cross, A. H., & Song, S. K. (2009). Axial diffusivity is the primary correlate of axonal injury in the experimental autoimmune encephalomyelitis spinal cord: a quantitative pixelwise analysis. *J Neurosci*, 29(9), 2805-2813. Retrieved from <https://www.ncbi.nlm.nih.gov/pubmed/19261876>. doi:10.1523/JNEUROSCI.4605-08.2009
- Chen, Y. J., Liu, C. M., Hsu, Y. C., Lo, Y. C., Hwang, T. J., Hwu, H. G., . . . Tseng, W. I. (2018). Individualized prediction of schizophrenia based on the whole-brain pattern of altered white matter tract integrity. *Hum Brain Mapp*, 39(1), 575-587. Retrieved from <https://www.ncbi.nlm.nih.gov/pubmed/29080229>. doi:10.1002/hbm.23867
- Chen, Y. J., Lo, Y. C., Hsu, Y. C., Fan, C. C., Hwang, T. J., Liu, C. M., . . . Tseng, W. Y. (2015). Automatic whole brain tract-based analysis using predefined tracts in a diffusion spectrum imaging template and an accurate registration strategy. *Hum Brain Mapp*, 36(9), 3441-3458. doi:10.1002/hbm.22854
- Chien, Y. L., Chen, Y. J., Hsu, Y. C., Tseng, W. I., & Gau, S. S. (2017). Altered white-matter integrity in unaffected siblings of probands with autism spectrum disorders.

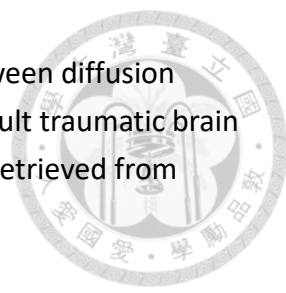
- 
- Hum Brain Mapp*, 38(12), 6053-6067. Retrieved from <http://www.ncbi.nlm.nih.gov/pubmed/28940697>. doi:10.1002/hbm.23810
- Concha, L., Gross, D. W., Wheatley, B. M., & Beaulieu, C. (2006). Diffusion tensor imaging of time-dependent axonal and myelin degradation after corpus callosotomy in epilepsy patients. *NeuroImage*, 32(3), 1090-1099. Retrieved from <https://www.ncbi.nlm.nih.gov/pubmed/16765064>. doi:10.1016/j.neuroimage.2006.04.187
- Cox, S. R., Ritchie, S. J., Tucker-Drob, E. M., Liewald, D. C., Hagenaars, S. P., Davies, G., . . . Deary, I. J. (2016). Ageing and brain white matter structure in 3,513 UK Biobank participants. *Nat Commun*, 7, 13629. doi:10.1038/ncomms13629
- Decker, M. W. (1987). The effects of aging on hippocampal and cortical projections of the forebrain cholinergic system. *Brain Res Rev*, 12, 423-438.
- Gold, B. T., & Keller, J. N. (Eds.). (2012). *Imaging Brain Aging and Neurodegenerative Disease*. (Vol. 1822).
- Ha, D. M., Xu, J., & Janowsky, J. S. (2007). Preliminary evidence that long-term estrogen use reduces white matter loss in aging. *Neurobiol Aging*, 28(12), 1936-1940. Retrieved from <https://www.ncbi.nlm.nih.gov/pubmed/17030475>. doi:10.1016/j.neurobiolaging.2006.08.007
- Hagmann, P., Cammoun, L., Gigandet, X., Meuli, R., Honey, C. J., Wedeen, V. J., & Sporns, O. (2008). Mapping the structural core of human cerebral cortex. *PLoS Biol*, 6(7), e159. Retrieved from <https://www.ncbi.nlm.nih.gov/pubmed/18597554>. doi:10.1371/journal.pbio.0060159
- Hsu, Y. C., Lo, Y. C., Chen, Y. J., Wedeen, V. J., & Isaac Tseng, W. Y. (2015). NTU-DSI-122: A diffusion spectrum imaging template with high anatomical matching to the ICBM-152 space. *Hum Brain Mapp*, 36(9), 3528-3541. Retrieved from <http://www.ncbi.nlm.nih.gov/pubmed/26095830>. doi:10.1002/hbm.22860
- Huang, J. Y., Liu, C. M., Hwang, T. J., Chen, Y. J., Hsu, Y. C., Hwu, H. G., . . . Tseng, W. I. (2018). Shared and distinct alterations of white matter tracts in remitted and nonremitted patients with schizophrenia. *Hum Brain Mapp*, 39(5), 2007-2019. Retrieved from <http://www.ncbi.nlm.nih.gov/pubmed/29377322>. doi:10.1002/hbm.23982
- Hugenschmidt, C. E., Peiffer, A. M., Kraft, R. A., Casanova, R., Deibler, A. R., Burdette, J. H., . . . Laurienti, P. J. (2008). Relating imaging indices of white matter integrity and volume in healthy older adults. *Cereb Cortex*, 18(2), 433-442. Retrieved from <http://www.ncbi.nlm.nih.gov/pubmed/17575289>. doi:10.1093/cercor/bhm080

- 
- Jang, S. H., & Seo, J. P. (2015). Aging of corticospinal tract fibers according to the cerebral origin in the human brain: a diffusion tensor imaging study. *Neurosci Lett*, 585, 77-81. Retrieved from <http://www.ncbi.nlm.nih.gov/pubmed/25445381>. doi:10.1016/j.neulet.2014.11.030
- Jelescu, I. O., Zurek, M., Winters, K. V., Veraart, J., Rajaratnam, A., Kim, N. S., . . . Fieremans, E. (2016). In vivo quantification of demyelination and recovery using compartment-specific diffusion MRI metrics validated by electron microscopy. *NeuroImage*, 132, 104-114. Retrieved from <https://www.ncbi.nlm.nih.gov/pubmed/26876473>. doi:10.1016/j.neuroimage.2016.02.004
- Kao, T. W., Hsu, Y. C., & Tseng, W. I. (2019). *Characteristic Normal Ageing Patterns of White Matter Tracts in 610 Cambridge Centre for Ageing and Neuroscience (Cam-CAN) Healthy Participants*. Paper presented at the International Society for Magnetic Resonance in Medicine Montreal, Canada.
- Le Bihan, D., & Lima, M. (2015). Diffusion Magnetic Resonance Imaging: What Water Tells Us about Biological Tissues. *PLoS Biol*, 13(7), e1002203. Retrieved from <https://www.ncbi.nlm.nih.gov/pubmed/26204162>. doi:10.1371/journal.pbio.1002203
- Lebel, C., Gee, M., Camicioli, R., Wieler, M., Martin, W., & Beaulieu, C. (2012). Diffusion tensor imaging of white matter tract evolution over the lifespan. *Neuroimage*, 60(1), 340-352. doi:10.1016/j.neuroimage.2011.11.094
- Liewald, D., Miller, R., Logothetis, N., Wagner, H. J., & Schuz, A. (2014). Distribution of axon diameters in cortical white matter: an electron-microscopic study on three human brains and a macaque. *Biol Cybern*, 108(5), 541-557. Retrieved from <http://www.ncbi.nlm.nih.gov/pubmed/25142940>. doi:10.1007/s00422-014-0626-2
- Lo, Y. C., Chen, Y. J., Hsu, Y. C., Chien, Y. L., Gau, S. S., & Tseng, W. I. (2019). Altered frontal aslant tracts as a heritable neural basis of social communication deficits in autism spectrum disorder: A sibling study using tract-based automatic analysis. *Autism Res*, 12(2), 225-238. Retrieved from <https://www.ncbi.nlm.nih.gov/pubmed/30548800>. doi:10.1002/aur.2044
- Lytelton, O., Boucher, M., Robbins, S., & Evans, A. (2007). An unbiased iterative group registration template for cortical surface analysis. *NeuroImage*, 34(4), 1535-1544. Retrieved from <https://www.ncbi.nlm.nih.gov/pubmed/17188895>. doi:10.1016/j.neuroimage.2006.10.041

- 
- Marner, L., & Pakkenberg, B. (2003). Total length of nerve fibers in prefrontal and global white matter of chronic schizophrenics. *Journal of Psychiatric Research*, 37(6), 539-547. doi:10.1016/s0022-3956(03)00069-4
- Meier-Ruge, W., Ulrich, J., Bruhlmann, M., & Meier, E. (1992). Age-Related White Matter Atrophy in the Human Brain. *Ann N Y Acad Sci*, 673, 260-269.
- Miller, K. L., Alfaro-Almagro, F., Bangerter, N. K., Thomas, D. L., Yacoub, E., Xu, J., . . . Smith, S. M. (2016). Multimodal population brain imaging in the UK Biobank prospective epidemiological study. *Nat Neurosci*, 19(11), 1523-1536. doi:10.1038/nn.4393
- Mora, F., & Phil, D. (2013). Successful brain aging: plasticity, environmental enrichment, and lifestyle. *Dialogues in Clinical Neuroscience*, 15(1), 45-52.
- Mosconi, L., Berti, V., Quinn, C., McHugh, P., Petrongolo, G., Varsavsky, I., . . . Brinton, R. D. (2017). Sex differences in Alzheimer risk. *Neurology*, 89, 1-9.
- Munoz Maniega, S., Chappell, F. M., Valdes Hernandez, M. C., Armitage, P. A., Makin, S. D., Heye, A. K., . . . Wardlaw, J. M. (2017). Integrity of normal-appearing white matter: Influence of age, visible lesion burden and hypertension in patients with small-vessel disease. *J Cereb Blood Flow Metab*, 37(2), 644-656. Retrieved from <https://www.ncbi.nlm.nih.gov/pubmed/26933133>. doi:10.1177/0271678X16635657
- O'Sullivan, M., Lythgoe, D. J., Pereira, A. C., Summers, P. E., Jarosz, J. M., Williams, S. C. R., & Markus, H. S. (2002). Patterns of cerebral blood flow reduction in patients with ischemic leukoaraiosis. *Neurology*, 59(3).
- Ozarslan, E., Koay, C. G., Shepherd, T. M., Komlos, M. E., Irfanoglu, M. O., Pierpaoli, C., & Basser, P. J. (2013). Mean apparent propagator (MAP) MRI: a novel diffusion imaging method for mapping tissue microstructure. *Neuroimage*, 78, 16-32. doi:10.1016/j.neuroimage.2013.04.016
- Pakkenberg, B., & Gundersen, H. J. (1997). Neocortical neuron number in humans: effect of sex and age. *Journal of Comparative Neurology*, 384, 312-320.
- Pakkenberg, B., Pelvig, D., Marner, L., Bundgaard, M. J., Gundersen, H. J., Nyengaard, J. R., & Regeur, L. (2003). Aging and the human neocortex. *Exp. Gerontol.*, 38, 95-99.
- Peper, J. S., van den Heuvel, M. P., Mandl, R. C., Hulshoff Pol, H. E., & van Honk, J. (2011). Sex steroids and connectivity in the human brain: a review of neuroimaging studies. *Psychoneuroendocrinology*, 36(8), 1101-1113. Retrieved from <https://www.ncbi.nlm.nih.gov/pubmed/21641727>. doi:10.1016/j.psyneuen.2011.05.004

- 
- Peters, A., & Folger, C. (2013). A website entitled "The fine structure of the aging brain". *J Comp Neurol*, 521(6), 1203-1206. Retrieved from <https://www.ncbi.nlm.nih.gov/pubmed/23229793>. doi:10.1002/cne.23280
- Peters, A., Morrison, J. H., Rosene, D. L., & Hyman, B. T. (1998). Feature Article Are Neurons Lost from the Primate Cerebral Cortex during Normal Aging? *Cereb Cortex*, 8, 295-300.
- Peters, A., Moss, M. B., & Sethares, C. (2000). Effects of Aging on Myelinated Nerve Fibers in Monkey Primary Visual Cortex. *Journal of Comparative Neurology*, 419, 364-376.
- Peters, A., & Sethares, C. (2002). Aging and the myelinated fibers in prefrontal cortex and corpus callosum of the monkey. *J Comp Neurol*, 442(3), 277-291. Retrieved from <http://www.ncbi.nlm.nih.gov/pubmed/11774342>.
- Prins, N. D., & Scheltens, P. (2015). White matter hyperintensities, cognitive impairment and dementia: an update. *Nature Reviews Neurology*, 11(3), 157-165. doi:10.1038/nrneurol.2015.10
- Reginold, W., Sam, K., Poubanc, J., Fisher, J., Crawley, A., & Mikulis, D. J. (2018). Impact of white matter hyperintensities on surrounding white matter tracts. *Neuroradiology*, 60(9), 933-944. Retrieved from <https://www.ncbi.nlm.nih.gov/pubmed/30030550>. doi:10.1007/s00234-018-2053-x
- Ritchie, S. J., Cox, S. R., Shen, X., Lombardo, M. V., Reus, L. M., Alloza, C., . . . Deary, I. J. (2018). Sex Differences in the Adult Human Brain: Evidence from 5216 UK Biobank Participants. *Cereb Cortex*, 28(8), 2959-2975. Retrieved from <http://www.ncbi.nlm.nih.gov/pubmed/29771288>. doi:10.1093/cercor/bhy109
- Ritchie, S. J., Tucker-Drob, E. M., Cox, S. R., Dickie, D. A., Del, C. V. H. M., Corley, J., . . . Deary, I. J. (2017). Risk and protective factors for structural brain ageing in the eighth decade of life. *Brain Struct Funct*, 222(8), 3477-3490. Retrieved from <https://www.ncbi.nlm.nih.gov/pubmed/28424895>. doi:10.1007/s00429-017-1414-2
- Rosenbluth, J., Stoffel, W., & Schiff, R. (1996). Myelin Structure in Proteolipid Protein (PLP)-Null Mouse Spinal Cord. *Journal of Comparative Neurology*, 371, 336-344.
- Schmidt, P., Gaser, C., Arsic, M., Buck, D., Forschler, A., Berthele, A., . . . Muhlau, M. (2012). An automated tool for detection of FLAIR-hyperintense white-matter lesions in Multiple Sclerosis. *Neuroimage*, 59(4), 3774-3783. doi:10.1016/j.neuroimage.2011.11.032
- Seltzer, B., Zolnouni, P., Nunez, M., Goldman, R., Kumar, D., Ieni, J., . . . Group, D. S. (2004). Efficacy of donepezil in early-stage Alzheimer disease: a randomized placebo-controlled trial. *Arch Neurol*, 61(12), 1852-1856.

- 
- Song, S.-K., Sun, S.-W., Ramsbottom, M. J., Chang, C., Russell, J., & Cross, A. H. (2002). Dismyelination Revealed through MRI as Increased Radial (but Unchanged Axial) Diffusion of Water. *NeuroImage*, 17(3), 1429-1436. doi:10.1006/nimg.2002.1267
- Sporns, O., Tononi, G., & Kotter, R. (2005). The human connectome: A structural description of the human brain. *PLoS Comput Biol*, 1(4), e42. Retrieved from <https://www.ncbi.nlm.nih.gov/pubmed/16201007>. doi:10.1371/journal.pcbi.0010042
- Stadlbauer, A., Salomonowitz, E., Strunk, G., Hammen, T., & Ganslandt, O. (2008). Assessment with Diffusion-Tensor Imaging and Quantitative Fiber Tracking. *Radiology*, 247, 179-188.
- Sudlow, C., Gallacher, J., Allen, N., Beral, V., Burton, P., Danesh, J., . . . Collins, R. (2015). UK biobank: an open access resource for identifying the causes of a wide range of complex diseases of middle and old age. *PLoS Med*, 12(3), e1001779. doi:10.1371/journal.pmed.1001779
- Sullivan, E. V., Adalsteinsson, E., & Pfefferbaum, A. (2006). Selective age-related degradation of anterior callosal fiber bundles quantified in vivo with fiber tracking. *Cereb Cortex*, 16, 1030-1039.
- Tian, Q., Glynn, N. W., Erickson, K. I., Aizenstein, H. J., Simonsick, E. M., Yaffe, K., . . . Health, A. B. C. S. (2015). Objective measures of physical activity, white matter integrity and cognitive status in adults over age 80. *Behav Brain Res*, 284, 51-57. Retrieved from <https://www.ncbi.nlm.nih.gov/pubmed/25655514>. doi:10.1016/j.bbr.2015.01.045
- Tomasi, D., & Volkow, N. D. (2012). Laterality patterns of brain functional connectivity: gender effects. *Cereb Cortex*, 22(6), 1455-1462. Retrieved from <https://www.ncbi.nlm.nih.gov/pubmed/21878483>. doi:10.1093/cercor/bhr230
- Tsai, T. H., Su, H. T., Hsu, Y. C., Shih, Y. C., Chen, C. C., Hu, F. R., & Tseng, W. I. (2019). White matter microstructural alterations in amblyopic adults revealed by diffusion spectrum imaging with systematic tract-based automatic analysis. *Br J Ophthalmol*, 103(4), 511-516. Retrieved from <https://www.ncbi.nlm.nih.gov/pubmed/29844086>. doi:10.1136/bjophthalmol-2017-311733
- Tuch, D. S. (2004). Q-ball imaging. *Magn Reson Med*, 52, 1358-1372.
- Waiter, G., Hsu, Y. C., Kang, Y. J., Kao, T. W., Chen, C. L., Chen, P. Y., & Tseng, W. I. (2019). *Microstructural changes of white matter tracts across late lifespan on 7,167 UK Biobank participants*. Paper presented at the Organization for Human Brain Mapping, Rome, Italy.

- 
- Wallace, E. J., Mathias, J. L., & Ward, L. (2018). The relationship between diffusion tensor imaging findings and cognitive outcomes following adult traumatic brain injury: A meta-analysis. *Neurosci Biobehav Rev*, 92, 93-103. Retrieved from <https://www.ncbi.nlm.nih.gov/pubmed/29803527>.
doi:10.1016/j.neubiorev.2018.05.023
- Williamson, W., Lewandowski, A. J., Forkert, N. D., Griffanti, L., Okell, T. W., Betts, J., . . . Leeson, P. (2018). Association of Cardiovascular Risk Factors With MRI Indices of Cerebrovascular Structure and Function and White Matter Hyperintensities in Young Adults. *JAMA*, 320(7), 665-673. Retrieved from <https://www.ncbi.nlm.nih.gov/pubmed/30140877>.
doi:10.1001/jama.2018.11498
- Wong, S. M., Jansen, J. F. A., Zhang, E., Hoff, E. I., Staals, J., van Oostenbrugge, R. J., & Backes, W. H. (2019). Blood-brain barrier impairment and hypoperfusion are linked in cerebral small vessel disease. *Neurology*, 92, e1-e9.
- Wu, C. H., Hwang, T. J., Chen, Y. J., Hsu, Y. C., Lo, Y. C., Liu, C. M., . . . Isaac Tseng, W. Y. (2015). Primary and secondary alterations of white matter connectivity in schizophrenia: A study on first-episode and chronic patients using whole-brain tractography-based analysis. *Schizophr Res*, 169(1-3), 54-61. Retrieved from <https://www.ncbi.nlm.nih.gov/pubmed/26443482>.
doi:10.1016/j.schres.2015.09.023
- Ycaza Herrera, A., & Mather, M. (2015). Actions and interactions of estradiol and glucocorticoids in cognition and the brain: Implications for aging women. *Neurosci Biobehav Rev*, 55, 36-52. Retrieved from <https://www.ncbi.nlm.nih.gov/pubmed/25929443>.
doi:10.1016/j.neubiorev.2015.04.005
- Yoon, B., Shim, Y. S., Lee, K. S., Shon, Y. M., & Yang, D. W. (2008). Region-specific changes of cerebral white matter during normal aging: a diffusion-tensor analysis. *Arch Gerontol Geriatr*, 47(1), 129-138. Retrieved from <https://www.ncbi.nlm.nih.gov/pubmed/17764763>.
doi:10.1016/j.archger.2007.07.004

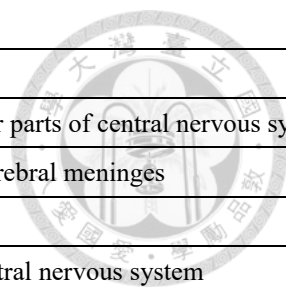
Supplementary Files

SF1. Screening of MRI data



UK Biobank makes all imaging data acquired available to researchers irrespective of quality. However, they have an automated QC pipeline that has been used to classify all data as “useable” or “unusable.” Details of the image quality control (QC) procedures applied by the UK Biobank before data release are detailed in Alfaro-Almagro et al. (Alfaro-Almagro et al., 2018). Parameters used to define “unusable” included; incorrect placement of Field of View; excessive head motion or noise; structurally atypical such as having important lesions; movement-related ringing or blurring; bias field or contrast problems. The total number of scans deemed useable by the UK Biobank automated QC procedure was 10102 for T1, 9756 for T2-FLAIR and 9566 for dMRI. The number of participants with useable scans from all three modalities was 8830.

International Classification of Diseases version 10 (ICD10) as provided by the UK Biobank (<https://biobank.ctsu.ox.ac.uk/crystal/field.cgi?id=41270>) was used to exclude participants diagnosed with neurological or psychiatric disease, substance abuse, or malignancy. Any participant with a diagnosis from one or more of the following categories was excluded:



ICD10 Coding	
Block C69-C72	C69-C72 Malignant neoplasms of eye, brain and other parts of central nervous system
Block C79	C79.3 Secondary malignant neoplasm of brain and cerebral meninges
Block D10	D10 Benign neoplasm of mouth and pharynx
Block D33	D 33 Benign neoplasm of brain and other parts of central nervous system
Block D36	D 36 Benign neoplasm of other and unspecified sites
Block F00-F09	F00-F09 Organic, including symptomatic, mental disorders
Block F10-F19	F10-F19 Mental and behavioural disorders due to psychoactive substance use
Block F20-F29	F20-F29 Schizophrenia, schizotypal and delusional disorders
Block F30-F39	F30-F39 Mood [affective] disorders
Block F40-F48	F40-F48 Neurotic, stress-related and somatoform disorders
Block F50-F59	F50-F59 Behavioural syndromes associated with psychological disturbances and physical factors
Block F60-F69	F60-F69 Disorders of adult personality and behaviour
Block F70-F79	F70-F79 Mental retardation
Block F80-F89	F80-F89 Disorders of psychological development
Block F90-F98	F90-F98 Behavioural and emotional disorders with onset usually occurring in childhood and adolescence
Block F99-F99	F99-F99 Unspecified mental disorder
Block G00-G09	G00-G09 Inflammatory diseases of the central nervous system
Block G10-G13	G10-G13 Systemic atrophies primarily affecting the central nervous system
Block G20-G26	G20-G26 Extrapyrimal and movement disorders
Block G30-G32	G30-G32 Other degenerative diseases of the central nervous system
Block G35-G37	G35-G37 Demyelinating diseases of the central nervous system
Block G40-G47	G40-G47 Episodic and paroxysmal disorders
Block G80-G83	G80-G83 Cerebral palsy and other paralytic syndromes
Block O00-O08	O00-O08 Pregnancy with abortive outcome
Block P00-P04	P00-P04 Foetus and newborn affected by maternal factors and by complications of pregnancy, labour and delivery
Block P05-P08	P05-P08 Disorders related to length of gestation and foetal growth
Block Q00-Q07	Q00-Q07 Congenital malformations of the nervous system
Block S00-S09	S00-S09 Injuries to the head
Block W65-W74	W65-W74 Accidental drowning and submersion
Block W75-W84	W75-W84 Other accidental threats to breathing
Block X40-X49	X40-X49 Accidental poisoning by and exposure to noxious substances

References: 1. Alfaro-Almagro, F., et al., *Image processing and Quality Control for the first 10,000 brain imaging datasets from UK Biobank*. Neuroimage, 2018. **166**: p. 400-424.

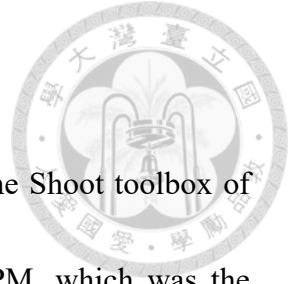
SF2. Procedures of image registration



To reduce the potential biases caused by registration, it would be better to conduct group-wise registration. Because there were several thousand participants enrolled in the study, they were processed in a hierarchical manner. In the subject level, the processing was conducted on the native data of each participant. Then the participants were divided into 60 groups, each comprised the same age and sex. In this group level, a group-wise registration procedure was conducted for each group. Finally, the 60 groups were considered as a single grand group. In the grand level, the mean of each group was registered to the ICBM-152 space, similar to the procedures employed in constructing NTU-DSI-122 in our previous work. In the following, the processing steps of each level were briefly introduced.

A. Subject level

1. For each participant, the diffusion data was aligned to T1w image by rigidly registered the b0 image to the T1w image using SPM12.
2. For each participant, the T1w image was segmented using SPM12. This step would result in tissue probability map (TPM) of gray matter (GM), white matter (WM) and cerebrospinal fluid (CSF). This step would also rigidly align the TPM to the MNI space.




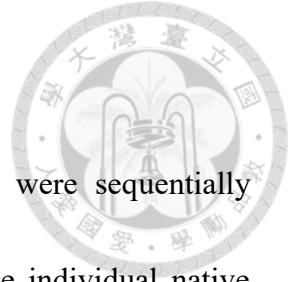
B. Group level

1. The TPMs of all participants were registered altogether using the Shoot toolbox of SPM12. This step would result in the group-specific mean TPM, which was the average of the individual TPMs in both shapes and values. The deformation maps (D1) associating the individual TPMs with the mean TPM were produced as well.
2. The D1 maps were used to transform the individual DTI, where the tensors were reoriented according to the deformation maps.
3. The registered DTI of step 2 were averaged to produce the intermediate DTI template.
4. The registered DTI of step 2 were further registered to the intermediate DTI template of step 3 using the LDDMM-DTI algorithm, resulting in another deformation maps D2.
5. The deformation maps D1 and D2 were combined and then used to transform the individual DTI. These registered DTI were averaged to produce the final group-specific DTI template.

C. Grand level

1. The group-specific mean TPMs were registered altogether using the Shoot toolbox of SPM12. This step would result in the grand mean TPM and the deformation maps (D3) which associated each TPM with the grand mean.

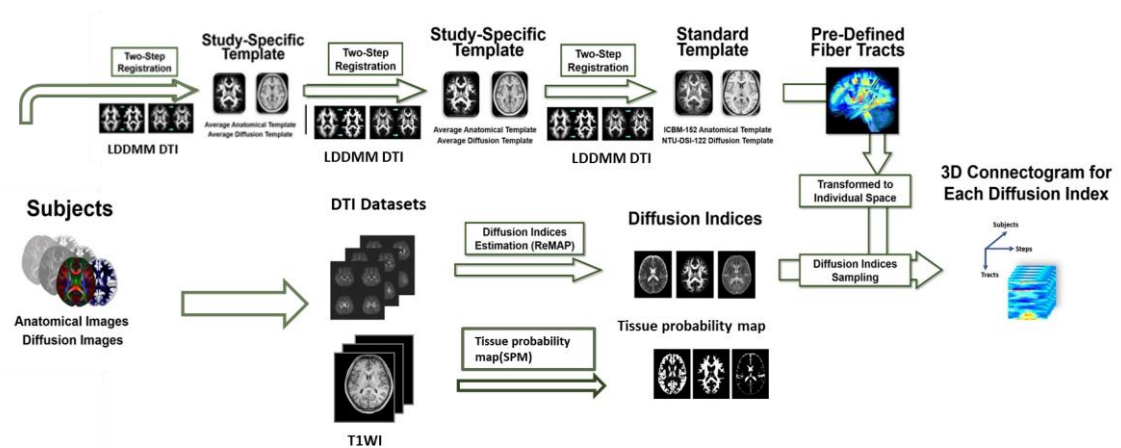
- 
2. The D3 maps were used to transform the group-specific DTI templates, where the tensors were reoriented according to the deformation maps.
 3. The registered DTI of step 2 were averaged to produce the intermediate grand DTI template.
 4. The registered DTI of step 2 were further registered to the intermediate grand DTI template using the LDDMM-DTI algorithm, resulting in another deformation maps D4.
 5. The deformation maps D3 and D4 were combined and then used to transform the group-specific DTI templates. These registered DTI were averaged to produce the final grand DTI template.
 6. The grand mean TPMs were registered to the ICBM-152 template using the DARTEL toolbox of SPM12. This step would result in the deformation map D5.
 7. The D5 map was used to transform the grand DTI template, where the tensors were reoriented according to the deformation map.
 8. The registered DTI of step 7 was further registered to the NTU-DSI-122-DTI template using the LDDMM-DTI algorithm, resulting in another deformation maps D6.



D. Combine the results across levels

1. For each participant, the deformation maps from D1 to D6 were sequentially combined, resulting in a deformation map which associated the individual native space to the ICBM-152 space.
2. The deformation map of step 1 was used to transform the white matter tract atlas, which was defined on the NTU-DSI-122 template, back to the individual space.

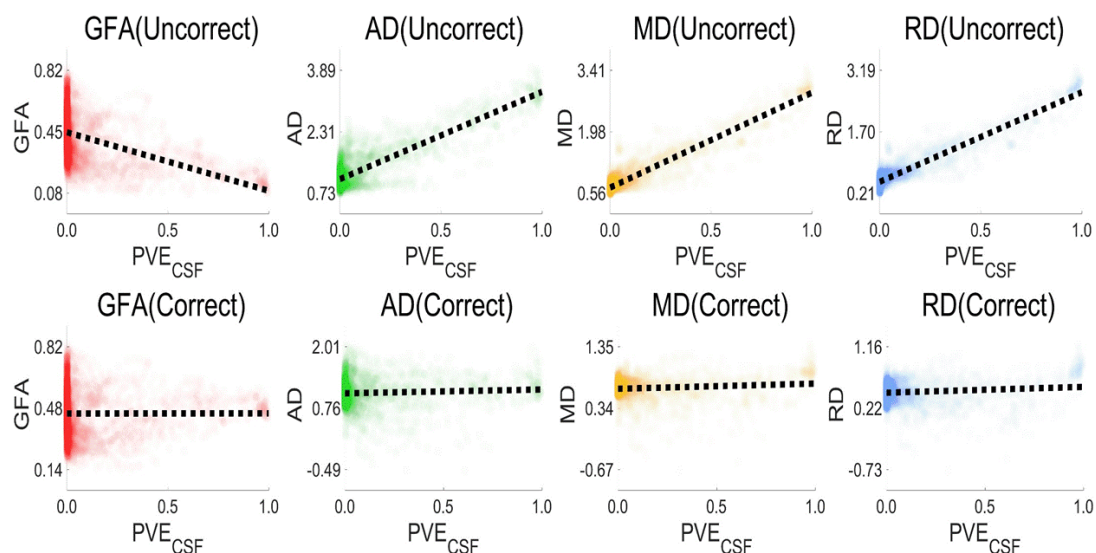
Figure SF2. The flow chart of tract-based automatic analysis (TBAA) procedures.



SF3. The results of diffusion indices after CSF partial volume correction as compared with uncorrected diffusion indices

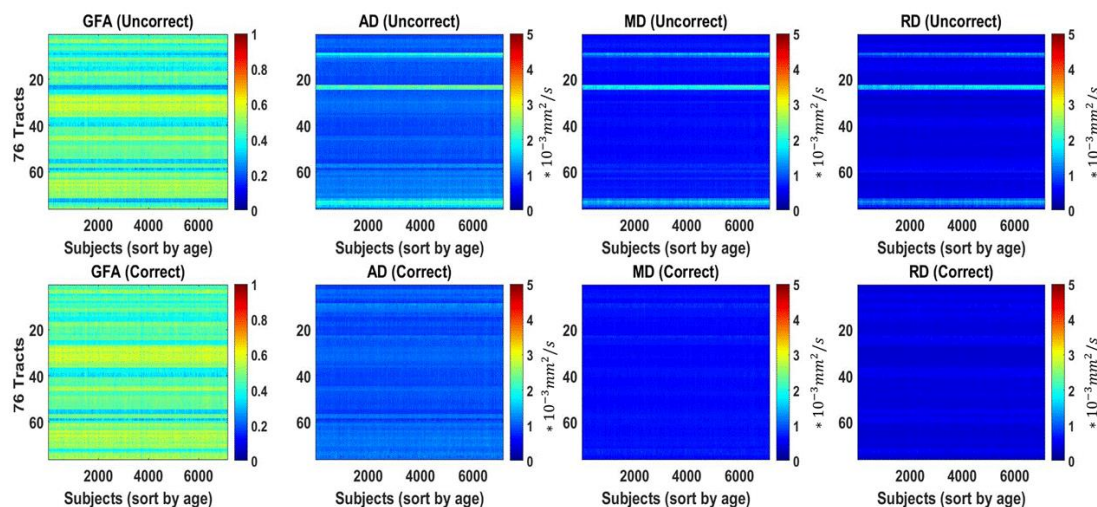
For each participant, we have a 76-by-100 array of the sampled diffusion indices (i.e., D_{app}) and a 76-by-100 array of CSF probabilities (i.e., V_{CSF}). We applied a linear regression model, $D_{app} = \beta_0 + \beta_1 V_{CSF}$, to regress 7600 values of D_{app} against 7600 values of V_{CSF} , and the model produced β_0 and β_1 for each participant. Corrected diffusion index (i.e., D_{WM}) at each step of the tract determined by subtracting $\beta_1 V_{CSF}$ from D_{app} in a stepwise manner. Figure SF3A demonstrates the results of linear regression on GFA, AD, RD, and MD in a participant.

Figure SF3A. Linear regression on GFA, AD, RD and MD values against V_{CSF} , before CSF partial volume correction (upper row) and after correction (lower row).

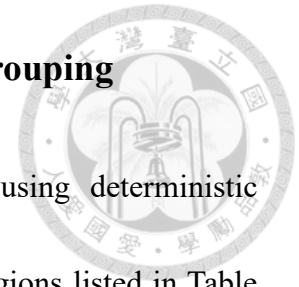


The same approach was applied to all participants to obtain corrected diffusion indices. Figure SF3B shows tract-based mean diffusion indices over all participants, before CSF partial volume correction as compared with those after correction. The tracts that showed abnormally high values of AD, RD, and MD and correspondingly low values of GFA were readily identified before correction (Figure SF3B, upper row). These tracts included bilateral fornices (tract number 9, 10), bilateral stria terminalis (tract number 23, 24) and the callosal fibers connecting bilateral temporal poles, hippocampus, amygdala, and precuneus (tract number 72, 73, 74, 75). The abnormal values were diminished after correction (Figure SF3B, lower row).

Figure SF3B. tract-mean diffusion indices over all participants, before CSF partial volume correction (upper row) and after correction (lower row).



SF4. Detailed information of 76 tracts and 5 levels of grouping



The 76 tracts were built in the NTU-DSI-122 template using deterministic tractography. The names of the tracts and the connected cortical regions listed in Table SF4. To appreciate the rate of change in tract property from the fine-grained level to the whole-brain level, the 76 tracts were grouped into 5 levels, i.e. 76 tracts, 25 tract groups, ten subsystems, three fiber systems, and a whole brain. In the 25 tract groups, the association fibers and projection fibers in the left and right hemispheres were averaged. In addition, SLFI, SLFII and SLFIII were merged into one tract group (SLF), and all CST subdivisions were merged into one tract group (CST). The frontostriatal tracts were merged into the tract group to the prefrontal cortex (FS_Pfc) and the tract group to the motor cortex (FS_Mot). The thalamic radiations were merged into four tract groups connecting the prefrontal cortex (TR_Pfc), sensorimotor cortex (TR_Sm), auditory cortex (TR_Aud) and visual cortex (TR_Opt). The callosal fibers were merged into 6 tract groups connecting the prefrontal cortex (CF_Pfc), sensorimotor cortex (CF_Sm), parietal cortex (CF_Par), occipital cortex (CF_Occ), temporal cortex (CF_Temp) and anterior/posterior commissures (CF_Comm). The ten subsystems merged the association fibers into two subsystems (the limbic and the cortical-cortical subsystems), merged the projection fibers into 3 subsystems (the corticospinal tract, frontostriatal and thalamic radiation subsystems), and merged the commissure fibers into 5 subsystems

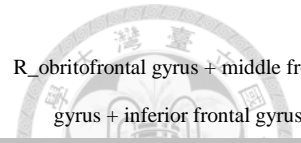
(anterior/posterior commissures, frontal, parietal, temporal and occipital subsystems).

The three fiber systems further merged the 10 subsystems into association, projection, and commissure fiber systems. Finally, the whole brain was the aggregate of three fiber systems. The hierarchy of 5 levels of tract grouping is shown in Figure SF4.

Table SF4. The names of the 76 tracts and the connected cortical regions.

Tracts	Full names	Connected ROIs	Connected ROIs
Association			
L CGB	L_cingulum of main body component	L_cingulate gyrus (anterior + middle parts)	L_cingulate gyrus posterior part
R CGB	R_cingulum of main body component	R_cingulate gyrus (anterior + middleparts)	R_cingulate gyrus posterior part
L CGH	L_cingulum of hippocampal component	L_cingulate gyrus posterior part	L_hippocampus
R CGH	R_cingulum of hippocampal component	R_cingulate gyrus posterior part	R_hippocampus
L FX	L_fornix	L_mammillary body	L_hippocampus
R FX	R_fornix	R_mammillary body	R_hippocampus
L ST	L_stria terminalis	L_septal nuclei	L_amygdala
R ST	R_stria terminalis	R_septal nuclei	R_amygdala
L UF	L_uncinate fasciculus	L_orbitofrontal gyrus	L_superior temporal pole
R UF	R_uncinate fasciculus	R_orbitofrontal gyrus	R_superior temporal pole
L AF	L_arcuate fasciculus	L_inferior frontal gyrus opercular part	L_superior temporal gyrus
R AF	R_arcuate fasciculus	R_inferior frontal gyrus opercular part	R_superior temporal gyrus
L FAT	L_frontal aslant tract	L_supplementary motor area	L_inferior frontal gyrus opercular part
R FAT	R_frontal aslant tract	R_supplementary motor area	R_inferior frontal gyrus opercular part
L IFOF	L_inferior fronto-occipital fasciculus	L_orbitofrontal gyrus	Occipital lobe
R IFOF	R_inferior fronto-occipital fasciculus	R_orbitofrontal gyrus	Occipital lobe
L ILF	L_inferior longitudinal fasciculus	L_temporal pole	Occipital lobe
R ILF	R_inferior longitudinal fasciculus	R_temporal pole	Occipital lobe
L PF	L_perpendicular fasciculus	L angular gyrus	L_fusiform gyrus
R PF	R_perpendicular fasciculus	R angular gyrus	R_fusiform gyrus
L SLF I	L_superior longitudinal fasciculus I	L_superior frontal gyrus	L_precuneus
R SLF I	R_superior longitudinal fasciculus I	R_superior frontal gyrus	R_precuneus
L SLF II	L_superior longitudinal fasciculus II	L_inferior frontal gyrus triangular part	L_middle occipital gyrus
R SLF II	R_superior longitudinal fasciculus II	R_inferior frontal gyrus triangular part	R_middle occipital gyrus
L SLF III	L_superior longitudinal fasciculus III	L_inferior frontal gyrus opercular part	L angular gyrus
R SLF III	R_superior longitudinal fasciculus III	R_inferior frontal gyrus opercular part	R angular gyrus

Projection			
L CST_Toe	L_ corticospinal tract of toe	Brain stem	L_primary motor cortex of toe component
R CST_Toe	R_ corticospinal tract of toe	Brain stem	R_primary motor cortex of toe component
L CST_Trunk	L_ corticospinal tract of trunk	Brain stem	L_ primary motor cortex of trunk component
R CST_Trunk	R_ corticospinal tract of trunk	Brain stem	R_ primary motor cortex of trunk component
L CST_Hand	L_ corticospinal tract of hand	Brain stem	L_primary motor cortex of hand component
R CST_Hand	R_ corticospinal tract of hand	Brain stem	R_ primary motor cortex of hand component
L CST_Mouth	L_ corticospinal tract of mouth	Brain stem	L_ primary motor cortex of mouth component
R CST_Mouth	R_ corticospinal tract of mouth	Brain stem	R_ primary motor cortex of mouth component
L CST_Geniculate	L_ corticospinal tract of geniculate fibers	Brain stem	L_primary motor cortex of throat component
R CST_Geniculate	R_ corticospinal tract of geniculate fibers	Brain stem	R_primary motor cortex of throat component
L ML	L_Medial lemniscus	Brain stem	L_thalamus
R ML	R_Medial lemniscus	Brain stem	R_thalamus
L FS_OFC	L_ frontal-striatum of orbitofrontal cortex	L_striatum (putamen + caudate)	L_orbitofrontal gyrus
R FS_OFC	R_ frontal-striatum of orbitofrontal cortex	R_striatum (putamen + caudate)	R_obritofrontal gyrus
L FS_VLPFC	L_ frontal-striatum of ventrolateral prefrontal cortex	L_striatum (putamen + caudate)	L_medial frontal gyrus + superior frontal gyrus
R FS_VLPFC	R_ frontal-striatum of ventrolateral prefrontal cortex	R_striatum (putamen + caudate)	R_medial frontal gyrus + superior frontal gyrus
L FS_DLPFC	L_ frontal-striatum of dorsolateral prefrontal cortex	L_striatum (putamen + caudate)	L_medial frontal gyrus + superior frontal gyrus
R FS_DLPFC	R_ frontal-striatum of dorsolateral prefrontal cortex	R_striatum (putamen + caudate)	R_medial frontal gyrus + superior frontal gyrus
L FS_Mot	L_ frontal-striatum of precentral gyrus	L_striatum (putamen + caudate)	L_precentral gyrus
R FS_Mot	R_ frontal-striatum of precentral gyrus	R_striatum (putamen + caudate)	R_precentral gyrus
L TR_VLPFC	L_ thalamic radiation of ventrolateral prefrontal cortex	L_thalamus	L_obritofrontal gyrus + middle frontal gyrus + inferior frontal gyrus

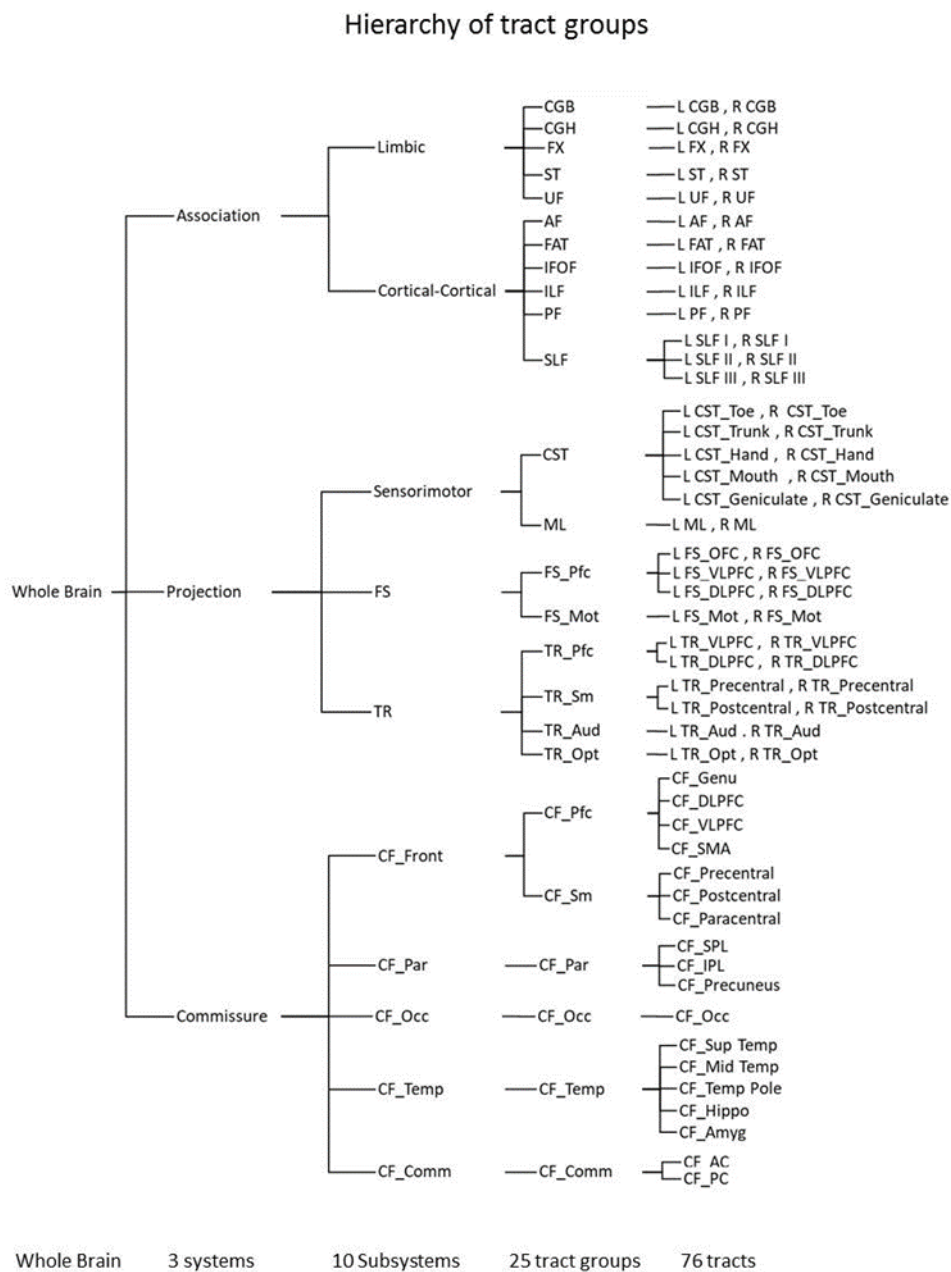


R TR_VLPFC	R_ thalamic radiation of ventrolateral prefrontal cortex	R_thalamus	R_orbitofrontal gyrus + middle frontal gyrus + inferior frontal gyrus
L TR_DLPFC	L_ thalamic radiation of dorsolateral prefrontal cortex	L_thalamus	L_medial frontal gyrus + superior frontal gyrus + supplementary motor area
R TR_DLPFC	R_ thalamic radiation of dorsolateral prefrontal cortex	R_thalamus	R_medial frontal gyrus + superior frontal gyrus + supplementary motor area
L TR_Precentral	L_ thalamic radiation of precentral gyrus	L_thalamus	L_precentral gyrus
R TR_Precentral	R_ thalamic radiation of precentral gyrus	R_thalamus	R_precentral gyrus
L TR_Postcentral	L_ thalamic radiation of postcentral gyrus	L_thalamus	L_postcentral gyrus
R TR_Postcentral	R_ thalamic radiation of postcentral gyrus	R_thalamus	R_postcentral gyrus
L TR_Aud	L_ thalamic radiation of auditory nerve	L_thalamus	L_Heschl's gyrus
R TR_Aud	R_ thalamic radiation of auditory nerve	R_thalamus	R_Heschl's gyrus
L TR_Opt	L_ thalamic radiation of optic radiation	L_thalamus	L_superior occipital gyrus
R TR_Opt	R_ thalamic radiation of optic radiation	R_thalamus	R_superior occipital gyrus
Commissure			
CF_Genu	Callosal fiber of genu	L_orbitofrontal gyrus	R_orbitofrontal gyrus
CF_DLPFC	Callosal fiber of Dorsolateral prefrontal cortex	L_medial frontal gyrus + superior frontal gyrus	R_medial frontal gyrus + superior frontal gyrus
CF_VLPFC	Callosal fiber of Ventrolateral prefrontal cortex	L_inferior frontal gyrus + middle frontal gyrus	R_inferior frontal gyrus + middle frontal gyrus
CF_SMA	Callosal fiber of supplementary motor areas	L_supplementary motor areas	R_supplementary motor areas
CF_Precentral	Callosal fiber of precentral gyrus	L_precentral gyrus	R_precentral gyrus
CF_Postcentral	Callosal fiber of postcentral gyrus	L_postcentral gyrus	R_postcentral gyrus
CF_Paracentral	Callosal fiber of paracentral lobule	L_paracentral lobules	R_paracentral lobules
CF_SPL	Callosal fiber of superior parietal lobule	L_superior parietal lobules	R_superior parietal lobules
CF_IPL	Callosal fiber of inferior parietal lobule	L_inferior parietal lobules	R_inferior parietal lobules
CF_Precuneus	Callosal fiber of precuneus	L_precuneus	R_precuneus
CF_Occ	Callosal fiber of occipital	L_occipital lobe	R_occipital lobe
CF_Sup Temp	Callosal fiber of superior temporal gyrus	L_superior temporal gyrus	R_superior temporal gyrus
CF_Mid Temp	Callosal fiber of middle temporal gyrus	L_middle temporal gyrus	R_middle temporal gyrus

CF_Temp Pole	Callosal fiber of temporal pole	L_temporal poles	R_temporal poles
CF_Hippo	Callosal fiber of hippocampus	L_hippocampus	R_hippocampus
CF_Amyg	Callosal fiber of amygdala	L_amygdala	R_amygdala
CF_AC	Anterior commissure	Front column of fornix	Bilateral cerebral hemispheres
CF_PC	Posterior commissure	L_cerebral hemisphere	R_cerebral hemisphere

L: left ; R: right ; ROI: region of interest

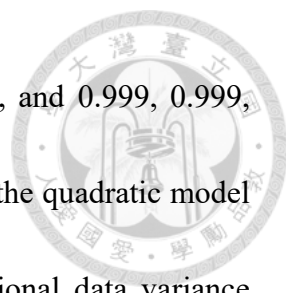
Figure SF4. Hierarchy of 5 levels of tract grouping



SF5. Justification of the use of the linear model as opposed to the quadratic model in the analysis of age-associated change in tract integrity



The normative model was built by calculating the mean and standard deviation of the diffusion index for each of the 76 tracts at each year of age from 47 to 76 (please see Supplementary File 8). The models were built for male and female participants separately. To test whether the linear model could adequately describe the age-associated change of the data, linear regression against age was performed for each tract using $Y = \beta_0 + \beta_1 \times \text{age}$, where Y indicated each participant's mean index value. Having obtained the fitted values of β_0 and β_1 , an estimated Y was calculated at each year of age. Pearson correlation was performed on the estimated Y at each year with the mean index values of the corresponding year in the normative model. The resulting correlation coefficients of GFA, AD, MD, RD and WMHL were very high in both male and female participants, 0.999, 0.998, 0.996, 0.997, and 0.897, respectively, for male, and 0.999, 0.998, 0.996, 0.998, and 0.900, respectively, for female subjects. For comparison, the data was also fitted by the quadratic model using $Y = \beta_0 + \beta_1 \times \text{age} + \beta_2 \times \text{age}^2$, and the estimated Y values were correlated with the mean index values of the corresponding year in the normative model. The resulting correlation coefficients of GFA, AD, MD, RD and WMHL were equally



high, 0.999, 0.999, 0.997, 0.998, and 0.911, respectively, for male, and 0.999, 0.999, 0.997, 0.998, and 0.918, respectively, for female subjects. Although the quadratic model fitted the data slightly better than did the linear model, the additional data variance explained by the quadratic model was only 2% at most. When the change of the index value across 30 years of age was of interest, β_1 extracted from either the linear model or the quadratic model was correlated with the average rate of change derived from the normative model. The average rate of change (Δavg) was calculated by $\Delta \text{avg} = (1/56) \sum [X(i+1) - X(i-1)]$, where $X(i)$ indicated the mean index value at age i ($i = 48, \dots, 75$) in the normative model. In the linear model, the correlation coefficients between β_1 and Δavg were consistently high for for GFA, AD, MD, RD and WMHI and both sexes, 0.944, 0.971, 0.967, 0.959, and 0.940, respectively, for male, and 0.873, 0.944, 0.958, 0.949, and 0.978, respectively, for female subjects. In the quadratic model, the correlation coefficients were generally low and inconsistent, 0.170, -0.428, -0.448, -0.317, and -0.414, respectively, for male, and -0.135, -0.566, -0.584, -0.497, and -0.825, respectively, for female subjects. Obviously, β_1 of the linear model described the age-associated change of the data more accurately than did β_1 of the quadratic model.

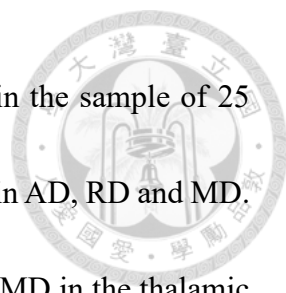
SF6. The β_1 and P values of GFA, AD, RD, and MD derived from the linear model at five levels of tract grouping



At the whole-brain level, both male and female participants showed a significant decrease in GFA and increased in AD, RD, and MD with age. At the three-system level, the trends were almost similar, except insignificant GFA change in the projection fiber system in male participants, and insignificant RD change in the commissure fiber system in male and female participants.

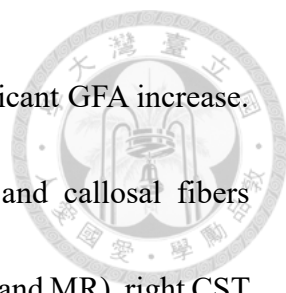
At the ten-subsystem level, a significant decrease in GFA and increased in AD, RD and MD with age were shown in most subsystems, but a few exceptions emerged. In male participants, significant age-related GFA increase was found in the callosal fibers connecting the temporal lobe (CF_Temp). Furthermore, a significant age-related decrease in RD was found in the callosal fibers connecting the occipital lobe (CF_Occ). In female participants, significant GFA increase with age was found in the anterior/posterior commissures (CF_Comm) and CF_Temp. Furthermore, a significant decrease in RD with age was found in CF_Temp.

At the level of 25 tract groups, more exceptions from the global trends were identified in addition to the ones revealed in the ten-subsystem level. In male participants, significant increase in GFA with age was identified in PF, ST, TR_Sm, and CF_Temp. In contrast, female participants did not show any tracts with significant age-associated increase in GFA. Although CF_Comm and CF_Temp still showed GFA increase with age,



they did not pass the statistical test after the Bonferroni correction in the sample of 25 tract groups. A few exceptions from the global trend were also found in AD, RD and MD. In male participants, the exceptions included decreased AD, RD and MD in the thalamic radiation to the visual cortex (TR_Opt) and PF, and decreased RD in CF_Occ. In female participants, the exceptions included decreased AD in the medial lemniscus (ML), decreased RD and MD in TR_Opt, and decreased RD in CF_Temp.

At the level of 76 tracts, more exceptions from the global trends were identified. In male participants, significant age-associated GFA increase was identified in left PF, left ST, bilateral CST connecting the hand region (CST_Hand), right CST to the mouth (CST_Mouth) and toe (CST_Toe) regions, bilateral thalamic radiations to the precentral (TR_Precentral) and postcentral (TR_Postcentral) regions, posterior commissure (CF_PC), callosal fibers connecting the superior temporal lobe (CF_Sup_temp), middle temporal lobe (CF_Mid_temp), temporal pole (CF_Temp_pole), and hippocampus (CF_Hippo). In female participants, significant age-associated GFA increase was identified in left TR_Postcentral, CF_Sup_temp, CF_Temp_pole and CF_Hippo. As for AD, RD or MD, exceptions were found in variable tracts. In male participants, significant decrease in AD, RD or MD was found in the tracts that showed significant GFA increase. These tracts included left PF (AD, RD and MD), left ST (AD and MD), bilateral CST_Hand, right CST_Toe, CF_Sup_temp and CF_Mid_temp (RD). There were also



tracts showing significant decrease in AD, RD or MD without significant GFA increase. These tracts included right PF (MD and RD), bilateral TR_Opt and callosal fibers connecting the ventrolateral prefrontal cortex (CF_VLPFC) (AD, RD and MR), right CST of the trunk (CST_Trunk), callosal fibers connecting the precuneus (CF_Precuneus) and CF_Occ (RD). In female participants, tracts that showed significant age-associated decrease in AD, RD or MD and significant increase in GFA included CF_Sup_temp, CF_Temp_pole and CF_Hippo (RD). Tracts that showed significant age-associated decrease in AD, RD or MD without significant GFA increase included right CST_Trunk and bilateral TR_Opt (MD and RD), left CST_Toe (AD and MD), left ML (AD), right ML (MD), CF_VLPFC (AD, RD and MD), callosal fibers connecting the precentral cortex (CF_Precentral) and precuneus (CF_Precuneus) (RD).

Table SF6. The rate of change in GFA, AD, RD, and MD in terms of β_1 and P values, male and female participants listed separately. The values are listed in sequence from the whole-brain, three-fiber-system, ten-subsystem, 25-tract-group level to the 76-tract levels, divided by thick lines. Four profiles of diffusion change are labeled in different colors: (1) the profile of decreased GFA and increased AD, RD, and MD with age is labeled in red, (2) the profile of increased AD, varied RD, increased MD and increased GFA with age is labeled in orange, (3) the profile of increase AD, decreased RD, increased GFA and

varied MD with age is labeled in green, and (4) the profile of decrease AD, decreased RD, decreased MD and varied GFA with age is labeled in blue. Only statistically significant β_1 values (figures in boldface) in either male or female participants were taken into consideration in categorizing the diffusion change profiles.

Note: Four profiles of diffusion change are labeled in different colors

ΔGFA	ΔAD	ΔRD	ΔMD
↓	↑	↑	↑
↑	↑	–	↑
↑	↑	↓	–
–	↓	↓	↓

$\beta_i \cdot 10^4$ (P-value)	GFA		AD $\cdot 10^{-3} \text{ mm}^2/\text{Sec}$		RD $\cdot 10^{-3} \text{ mm}^2/\text{Sec}$		MD $\cdot 10^{-3} \text{ mm}^2/\text{Sec}$	
	M	F	M	F	M	F	M	F
Whole brain	-1.22 (0.000)	-2.99 (0.000)	8.64 (0.000)	6.11 (0.000)	3.51 (0.000)	4.46 (0.000)	5.22 (0.000)	5.01 (0.000)
Association	-1.92 (0.000)	-3.62 (0.000)	7.28 (0.000)	6.06 (0.000)	5.69 (0.000)	7.18 (0.000)	6.22 (0.000)	6.80 (0.000)
Projection	-0.25 (0.444)	-2.67 (0.000)	10.38 (0.000)	7.39 (0.000)	3.02 (0.000)	4.65 (0.000)	5.47 (0.000)	5.56 (0.000)
Commissure	-1.92 (0.000)	-2.68 (0.000)	7.53 (0.000)	3.93 (0.000)	1.23 (0.018)	0.21 (0.659)	3.33 (0.000)	1.45 (0.003)
Limbic	-1.06 (0.004)	-2.77 (0.000)	9.23 (0.000)	6.86 (0.000)	8.46 (0.000)	9.44 (0.000)	8.71 (0.000)	8.58 (0.000)
Cortical-Cortical	-2.46 (0.000)	-4.15 (0.000)	6.07 (0.000)	5.56 (0.000)	3.97 (0.000)	5.76 (0.000)	4.67 (0.000)	5.70 (0.000)
Sensorimotor	0.88 (0.011)	-1.50 (0.000)	4.19 (0.000)	-0.07 (0.907)	-0.85 (0.026)	0.29 (0.426)	0.83 (0.014)	0.17 (0.608)
FS	-2.33 (0.000)	-5.02 (0.000)	17.73 (0.000)	16.07 (0.000)	9.66 (0.000)	11.84 (0.000)	12.35 (0.000)	13.25 (0.000)
TR	0.02 (0.963)	-2.26 (0.000)	11.66 (0.000)	9.06 (0.000)	2.47 (0.000)	4.21 (0.000)	5.54 (0.000)	5.83 (0.000)
CF_Front	-7.08 (0.000)	-7.75 (0.000)	3.04 (0.001)	-0.08 (0.930)	3.57 (0.000)	3.25 (0.000)	3.39 (0.000)	2.14 (0.001)
CF_Par	-2.75 (0.000)	-3.02 (0.000)	6.67 (0.000)	5.04 (0.000)	2.13 (0.001)	1.20 (0.040)	3.65 (0.000)	2.48 (0.000)
CF_Occ	-1.57 (0.013)	-2.79 (0.000)	0.74 (0.530)	1.19 (0.301)	-2.72 (0.001)	-0.25 (0.756)	-1.57 (0.028)	0.23 (0.735)
CF_Temp	3.02 (0.000)	1.08 (0.003)	13.07 (0.000)	5.07 (0.000)	-0.78 (0.352)	-3.94 (0.000)	3.84 (0.000)	-0.93 (0.215)
CF_Comm	0.50 (0.371)	1.49 (0.003)	10.46 (0.000)	9.64 (0.000)	0.13 (0.870)	0.77 (0.300)	3.57 (0.000)	3.73 (0.000)
CGB	-0.08 (0.913)	-2.44 (0.000)	5.66 (0.000)	5.70 (0.000)	3.76 (0.000)	5.80 (0.000)	4.39 (0.000)	5.77 (0.000)
CGH	-0.82 (0.096)	-2.47 (0.000)	8.06 (0.000)	6.43 (0.000)	5.19 (0.000)	6.87 (0.000)	6.15 (0.000)	6.72 (0.000)
FX	-3.08 (0.000)	-3.64 (0.000)	25.26 (0.000)	7.70 (0.000)	16.45 (0.000)	5.46 (0.000)	19.38 (0.000)	6.21 (0.000)
ST	2.50 (0.000)	-0.71 (0.133)	-2.42 (0.062)	7.63 (0.000)	8.92 (0.000)	21.67 (0.000)	5.14 (0.000)	16.99 (0.000)
UF	-3.81 (0.000)	-4.57 (0.000)	9.58 (0.000)	6.81 (0.000)	7.98 (0.000)	7.38 (0.000)	8.51 (0.000)	7.19 (0.000)
AF	-2.31 (0.000)	-4.17 (0.000)	10.49 (0.000)	10.03 (0.000)	4.00 (0.000)	6.25 (0.000)	6.17 (0.000)	7.51 (0.000)
FAT	-1.92 (0.000)	-5.33 (0.000)	10.69 (0.000)	7.32 (0.000)	6.39 (0.000)	8.44 (0.000)	7.82 (0.000)	8.06 (0.000)
IFOF	-7.20 (0.000)	-7.36 (0.000)	2.79 (0.000)	3.95 (0.000)	8.88 (0.000)	9.08 (0.000)	6.85 (0.000)	7.37 (0.000)
ILF	-3.65 (0.000)	-3.24 (0.000)	10.07 (0.000)	9.79 (0.000)	6.18 (0.000)	5.91 (0.000)	7.48 (0.000)	7.21 (0.000)
PF	1.79 (0.000)	-1.16 (0.014)	-3.47 (0.000)	-0.76 (0.380)	-6.66 (0.000)	-0.69 (0.327)	-5.60 (0.000)	-0.71 (0.284)
SLF	-2.14 (0.000)	-3.98 (0.000)	5.99 (0.000)	4.72 (0.000)	4.31 (0.000)	5.70 (0.000)	4.87 (0.000)	5.38 (0.000)
CST	0.99 (0.006)	-1.58 (0.000)	5.19 (0.000)	0.51 (0.379)	-0.93 (0.019)	0.36 (0.348)	1.11 (0.001)	0.40 (0.229)
ML	0.33 (0.432)	-1.07 (0.010)	-0.81 (0.346)	-2.94 (0.000)	-0.46 (0.316)	-0.01 (0.978)	-0.57 (0.230)	-0.97 (0.036)
FS_Pfc	-2.50 (0.000)	-4.98 (0.000)	18.50 (0.000)	16.59 (0.000)	10.06 (0.000)	11.97 (0.000)	12.87 (0.000)	13.51 (0.000)
FS_Mot	-1.85 (0.000)	-5.13 (0.000)	15.44 (0.000)	14.52 (0.000)	8.45 (0.000)	11.44 (0.000)	10.78 (0.000)	12.47 (0.000)
TR_Pfc	-2.28 (0.000)	-4.86 (0.000)	20.84 (0.000)	17.49 (0.000)	8.80 (0.000)	10.47 (0.000)	12.81 (0.000)	12.81 (0.000)
TR_Sm	4.46 (0.000)	0.88 (0.075)	15.76 (0.000)	10.22 (0.000)	0.38 (0.495)	2.44 (0.000)	5.50 (0.000)	5.03 (0.000)
TR_Aud	-1.57 (0.000)	-2.47 (0.000)	4.62 (0.000)	1.43 (0.012)	3.61 (0.000)	3.54 (0.000)	3.94 (0.000)	2.84 (0.000)
TR_Opt	-2.69 (0.000)	-3.14 (0.000)	-7.81 (0.000)	-2.46 (0.025)	-7.13 (0.000)	-4.07 (0.000)	-7.36 (0.000)	-3.53 (0.000)
CF_Pfc	-8.54 (0.000)	-9.15 (0.000)	0.97 (0.284)	-0.96 (0.271)	5.00 (0.000)	5.08 (0.000)	3.66 (0.000)	3.07 (0.000)
CF_Sm	-3.60 (0.000)	-3.88 (0.000)	5.58 (0.000)	3.89 (0.000)	2.85 (0.000)	2.21 (0.000)	3.76 (0.000)	2.77 (0.000)
CF_Par	-1.40 (0.006)	-1.86 (0.000)	9.30 (0.000)	5.66 (0.000)	-0.01 (0.990)	-1.56 (0.021)	3.09 (0.000)	0.84 (0.272)
CF_Occ	-1.57 (0.013)	-2.79 (0.000)	0.74 (0.530)	1.19 (0.301)	-2.72 (0.001)	-0.25 (0.756)	-1.57 (0.028)	0.23 (0.735)
CF_Temp	3.02 (0.000)	1.08 (0.003)	13.07 (0.000)	5.07 (0.000)	-0.78 (0.352)	-3.94 (0.000)	3.84 (0.000)	-0.93 (0.215)
CF_Comm	0.50 (0.371)	1.49 (0.003)	10.46 (0.000)	9.64 (0.000)	0.13 (0.870)	0.77 (0.300)	3.57 (0.000)	3.73 (0.000)

L CGB	-1.38 (0.080)	-2.97 (0.000)	3.14 (0.017)	4.26 (0.000)	4.46 (0.000)	5.92 (0.000)	4.02 (0.000)	5.37 (0.000)
R CGB	1.23 (0.137)	-1.90 (0.017)	8.18 (0.000)	7.14 (0.000)	3.05 (0.000)	5.68 (0.000)	4.76 (0.000)	6.16 (0.000)
L CGH	-0.04 (0.954)	-2.27 (0.000)	5.94 (0.000)	1.87 (0.065)	2.23 (0.008)	3.06 (0.000)	3.47 (0.000)	2.66 (0.000)
R CGH	-1.61 (0.003)	-2.68 (0.000)	10.17 (0.000)	10.99 (0.000)	8.15 (0.000)	10.68 (0.000)	8.82 (0.000)	10.78 (0.000)
L FX	-0.22 (0.677)	-2.14 (0.000)	31.03 (0.000)	11.90 (0.000)	10.39 (0.000)	2.17 (0.128)	17.27 (0.000)	5.41 (0.000)
R FX	-5.94 (0.000)	-5.14 (0.000)	19.48 (0.000)	3.51 (0.017)	22.51 (0.000)	8.76 (0.000)	21.50 (0.000)	7.01 (0.000)
L ST	3.75 (0.000)	-0.22 (0.670)	-17.41 (0.000)	2.84 (0.076)	0.07 (0.964)	21.10 (0.000)	-5.76 (0.000)	15.01 (0.000)
R ST	1.25 (0.013)	-1.20 (0.014)	12.58 (0.000)	12.42 (0.000)	17.78 (0.000)	22.25 (0.000)	16.04 (0.000)	18.97 (0.000)
L UF	-3.46 (0.000)	-3.67 (0.000)	10.15 (0.000)	8.05 (0.000)	7.57 (0.000)	6.85 (0.000)	8.43 (0.000)	7.25 (0.000)
R UF	-4.16 (0.000)	-5.48 (0.000)	9.01 (0.000)	5.58 (0.000)	8.39 (0.000)	7.90 (0.000)	8.60 (0.000)	7.13 (0.000)
L AF	-3.34 (0.000)	-5.47 (0.000)	10.00 (0.000)	9.23 (0.000)	4.75 (0.000)	7.19 (0.000)	6.50 (0.000)	7.87 (0.000)
R AF	-1.29 (0.026)	-2.87 (0.000)	10.99 (0.000)	10.82 (0.000)	3.26 (0.000)	5.31 (0.000)	5.84 (0.000)	7.15 (0.000)
L FAT	-4.11 (0.000)	-7.75 (0.000)	13.57 (0.000)	9.03 (0.000)	9.22 (0.000)	11.81 (0.000)	10.67 (0.000)	10.88 (0.000)
R FAT	0.27 (0.629)	-2.91 (0.000)	7.80 (0.000)	5.61 (0.000)	3.56 (0.000)	5.07 (0.000)	4.97 (0.000)	5.25 (0.000)
L IFOF	-8.17 (0.000)	-8.04 (0.000)	0.48 (0.539)	2.55 (0.001)	8.91 (0.000)	9.06 (0.000)	6.10 (0.000)	6.89 (0.000)
R IFOF	-6.22 (0.000)	-6.68 (0.000)	5.10 (0.000)	5.35 (0.000)	8.84 (0.000)	9.11 (0.000)	7.59 (0.000)	7.86 (0.000)
L ILF	-2.00 (0.011)	-2.53 (0.001)	10.70 (0.000)	9.27 (0.000)	4.44 (0.000)	4.93 (0.000)	6.53 (0.000)	6.37 (0.000)
R ILF	-5.30 (0.000)	-3.95 (0.000)	9.45 (0.000)	10.31 (0.000)	7.91 (0.000)	6.90 (0.000)	8.42 (0.000)	8.04 (0.000)
L PF	3.71 (0.000)	-0.80 (0.141)	-4.40 (0.000)	-3.69 (0.000)	-9.70 (0.000)	-3.47 (0.000)	-7.94 (0.000)	-3.55 (0.000)
R PF	-0.13 (0.813)	-1.51 (0.007)	-2.54 (0.013)	2.18 (0.029)	-3.62 (0.000)	2.10 (0.006)	-3.26 (0.000)	2.12 (0.003)
L SLF I	-2.22 (0.000)	-5.74 (0.000)	5.16 (0.000)	2.18 (0.041)	4.77 (0.000)	7.07 (0.000)	4.90 (0.000)	5.44 (0.000)
R SLF I	-5.37 (0.000)	-6.64 (0.000)	4.25 (0.000)	2.44 (0.020)	8.02 (0.000)	8.78 (0.000)	6.76 (0.000)	6.66 (0.000)
L SLF II	-1.63 (0.008)	-2.87 (0.000)	6.85 (0.000)	6.08 (0.000)	3.76 (0.000)	4.80 (0.000)	4.79 (0.000)	5.22 (0.000)
R SLF II	0.27 (0.650)	-1.41 (0.013)	7.02 (0.000)	7.29 (0.000)	1.53 (0.011)	3.84 (0.000)	3.36 (0.000)	4.99 (0.000)
L SLF III	-2.81 (0.000)	-3.76 (0.000)	8.05 (0.000)	8.02 (0.000)	5.92 (0.000)	7.02 (0.000)	6.63 (0.000)	7.35 (0.000)
R SLF III	-1.08 (0.141)	-3.44 (0.000)	4.58 (0.000)	2.29 (0.031)	1.88 (0.006)	2.72 (0.000)	2.78 (0.000)	2.58 (0.000)
L CST_Toe	0.25 (0.605)	-2.42 (0.000)	1.07 (0.208)	-3.82 (0.000)	-1.13 (0.018)	-0.10 (0.828)	-0.38 (0.319)	-1.32 (0.001)
R CST_Toe	2.34 (0.000)	-0.26 (0.559)	4.23 (0.000)	-0.31 (0.674)	-3.66 (0.000)	-2.09 (0.000)	-1.00 (0.022)	-1.46 (0.001)
L CST_Trunk	0.39 (0.463)	-2.82 (0.000)	4.16 (0.000)	-1.28 (0.110)	-0.24 (0.619)	1.54 (0.001)	1.19 (0.001)	0.53 (0.143)
R CST_Trunk	1.48 (0.001)	-0.66 (0.128)	4.30 (0.000)	-1.60 (0.049)	-5.32 (0.000)	-5.31 (0.000)	-2.11 (0.001)	-4.07 (0.000)
L CST_Hand	2.25 (0.000)	-0.54 (0.174)	8.37 (0.000)	3.17 (0.000)	-1.95 (0.000)	-0.28 (0.524)	1.49 (0.000)	0.88 (0.019)
R CST_Hand	3.61 (0.000)	0.60 (0.166)	8.11 (0.000)	2.74 (0.000)	-1.91 (0.000)	-0.25 (0.565)	1.42 (0.000)	0.71 (0.046)
L CST_Mouth	1.36 (0.002)	-1.96 (0.000)	4.36 (0.000)	-0.54 (0.486)	-1.08 (0.029)	1.44 (0.005)	0.67 (0.127)	0.74 (0.109)
R CST_Mouth	1.67 (0.001)	-0.82 (0.075)	5.89 (0.000)	-0.37 (0.661)	-1.55 (0.005)	-0.92 (0.113)	0.94 (0.044)	-0.75 (0.137)
L CST_Geniculate	-1.42 (0.000)	-3.27 (0.000)	5.15 (0.000)	2.61 (0.000)	3.58 (0.000)	4.53 (0.000)	4.11 (0.000)	3.89 (0.000)
R CST_Geniculate	-2.04 (0.000)	-3.69 (0.000)	6.21 (0.000)	4.48 (0.000)	4.01 (0.000)	5.00 (0.000)	4.74 (0.000)	4.85 (0.000)
L ML	-0.83 (0.069)	-2.06 (0.000)	-2.07 (0.030)	-3.15 (0.001)	0.81 (0.106)	1.31 (0.007)	-0.11 (0.837)	-0.14 (0.777)
R ML	1.49 (0.002)	-0.08 (0.868)	0.45 (0.610)	-2.73 (0.001)	-1.73 (0.001)	-1.34 (0.010)	-1.02 (0.040)	-1.80 (0.000)
L FS_OFC	-2.95 (0.000)	-3.48 (0.000)	8.21 (0.000)	8.32 (0.000)	5.72 (0.000)	6.26 (0.000)	6.55 (0.000)	6.94 (0.000)
R FS_OFC	-4.06 (0.000)	-3.61 (0.000)	9.16 (0.000)	8.68 (0.000)	7.29 (0.000)	6.22 (0.000)	7.91 (0.000)	7.04 (0.000)

L FS_VLPFC	-1.22 (0.089)	-5.64 (0.000)	25.36 (0.000)	24.68 (0.000)	14.95 (0.000)	19.26 (0.000)	18.42 (0.000)	21.06 (0.000)
R FS_VLPFC	-0.96 (0.165)	-5.10 (0.000)	24.34 (0.000)	23.20 (0.000)	13.54 (0.000)	17.50 (0.000)	17.14 (0.000)	19.40 (0.000)
L FS_DLPFC	-2.88 (0.000)	-5.51 (0.000)	21.62 (0.000)	18.14 (0.000)	9.82 (0.000)	11.36 (0.000)	13.75 (0.000)	13.62 (0.000)
R FS_DLPFC	-2.91 (0.000)	-6.55 (0.000)	22.29 (0.000)	16.51 (0.000)	9.03 (0.000)	11.20 (0.000)	13.45 (0.000)	12.97 (0.000)
L FS_Mot	-1.70 (0.004)	-5.37 (0.000)	14.82 (0.000)	14.39 (0.000)	7.95 (0.000)	11.75 (0.000)	10.24 (0.000)	12.63 (0.000)
R FS_Mot	-1.99 (0.001)	-4.90 (0.000)	16.07 (0.000)	14.65 (0.000)	8.95 (0.000)	11.14 (0.000)	11.32 (0.000)	12.31 (0.000)
L TR_VLPFC	-3.33 (0.000)	-6.06 (0.000)	20.07 (0.000)	17.99 (0.000)	9.98 (0.000)	12.17 (0.000)	13.34 (0.000)	14.11 (0.000)
R TR_VLPFC	-3.19 (0.000)	-4.35 (0.000)	21.35 (0.000)	20.24 (0.000)	11.24 (0.000)	11.88 (0.000)	14.61 (0.000)	14.67 (0.000)
L TR_DLPFC	-1.44 (0.001)	-4.51 (0.000)	20.60 (0.000)	15.86 (0.000)	6.92 (0.000)	8.81 (0.000)	11.48 (0.000)	11.16 (0.000)
R TR_DLPFC	-1.17 (0.007)	-4.53 (0.000)	21.32 (0.000)	15.86 (0.000)	7.07 (0.000)	9.00 (0.000)	11.82 (0.000)	11.28 (0.000)
L TR_Precentral	3.34 (0.000)	-0.74 (0.215)	15.01 (0.000)	10.03 (0.000)	2.15 (0.000)	4.84 (0.000)	6.44 (0.000)	6.57 (0.000)
R TR_Precentral	4.13 (0.000)	0.12 (0.830)	17.55 (0.000)	11.50 (0.000)	1.88 (0.001)	4.30 (0.000)	7.10 (0.000)	6.70 (0.000)
L TR_Postcentral	5.37 (0.000)	2.55 (0.000)	14.18 (0.000)	8.06 (0.000)	-2.25 (0.001)	-1.43 (0.027)	3.22 (0.000)	1.73 (0.004)
R TR_Postcentral	5.00 (0.000)	1.57 (0.003)	16.28 (0.000)	11.30 (0.000)	-0.26 (0.673)	2.04 (0.001)	5.26 (0.000)	5.13 (0.000)
L TR_Aud	-2.23 (0.000)	-3.01 (0.000)	2.53 (0.000)	0.25 (0.694)	2.58 (0.000)	3.07 (0.000)	2.56 (0.000)	2.13 (0.000)
R TR_Aud	-0.91 (0.033)	-1.92 (0.000)	6.70 (0.000)	2.61 (0.000)	4.64 (0.000)	4.01 (0.000)	5.33 (0.000)	3.54 (0.000)
L TR_Opt	-2.99 (0.000)	-3.33 (0.000)	-8.68 (0.000)	-2.24 (0.069)	-7.90 (0.000)	-4.36 (0.000)	-8.16 (0.000)	-3.65 (0.000)
R TR_Opt	-2.39 (0.000)	-2.95 (0.000)	-6.94 (0.000)	-2.69 (0.026)	-6.37 (0.000)	-3.77 (0.000)	-6.56 (0.000)	-3.41 (0.000)
CF_Genu	-10.61 (0.000)	-10.72 (0.000)	0.41 (0.680)	-0.48 (0.622)	8.19 (0.000)	8.47 (0.000)	5.59 (0.000)	5.49 (0.000)
CF_DLPFC	-10.65 (0.000)	-10.97 (0.000)	7.55 (0.000)	8.32 (0.000)	15.13 (0.000)	15.08 (0.000)	12.61 (0.000)	12.83 (0.000)
CF_VLPFC	-5.29 (0.000)	-7.07 (0.000)	-9.31 (0.000)	-17.07 (0.000)	-13.34 (0.000)	-13.04 (0.000)	-12.00 (0.000)	-14.38 (0.000)
CF_SMA	-7.59 (0.000)	-7.83 (0.000)	5.24 (0.000)	5.40 (0.000)	10.01 (0.000)	9.82 (0.000)	8.42 (0.000)	8.35 (0.000)
CF_Precentral	-1.28 (0.004)	-2.14 (0.000)	11.29 (0.000)	3.45 (0.001)	-2.13 (0.011)	-4.07 (0.000)	2.34 (0.007)	-1.56 (0.050)
CF_Postcentral	-2.63 (0.000)	-3.77 (0.000)	7.97 (0.000)	7.12 (0.000)	4.37 (0.000)	5.11 (0.000)	5.57 (0.000)	5.78 (0.000)
CF_Paracentral	-6.90 (0.000)	-5.74 (0.000)	-2.52 (0.015)	1.10 (0.288)	6.33 (0.000)	5.59 (0.000)	3.38 (0.000)	4.09 (0.000)
CF_SPL	-3.47 (0.000)	-4.13 (0.000)	9.12 (0.000)	8.20 (0.000)	5.45 (0.000)	6.91 (0.000)	6.67 (0.000)	7.34 (0.000)
CF_IPL	1.10 (0.037)	-0.75 (0.134)	22.45 (0.000)	15.12 (0.000)	-0.21 (0.788)	-0.78 (0.310)	7.34 (0.000)	4.52 (0.000)
CF_Precuneus	-1.82 (0.046)	-0.68 (0.464)	-3.65 (0.274)	-6.35 (0.051)	-5.26 (0.000)	-10.82 (0.000)	-4.73 (0.006)	-9.33 (0.000)
CF_Occ	-1.57 (0.013)	-2.79 (0.000)	0.74 (0.530)	1.19 (0.301)	-2.72 (0.001)	-0.25 (0.756)	-1.57 (0.028)	0.23 (0.735)
CF_Sup Temp	3.62 (0.000)	1.95 (0.000)	21.16 (0.000)	12.55 (0.000)	-5.98 (0.000)	-7.21 (0.000)	3.06 (0.000)	-0.62 (0.423)
CF_Mid Temp	2.94 (0.000)	0.19 (0.686)	8.44 (0.000)	8.08 (0.000)	-8.06 (0.000)	-3.70 (0.000)	-2.56 (0.001)	0.23 (0.754)
CF_Temp Pole	4.01 (0.000)	1.73 (0.000)	5.83 (0.000)	-5.33 (0.000)	-3.24 (0.006)	-9.35 (0.000)	-0.22 (0.854)	-8.01 (0.000)
CF_Hippo	4.63 (0.000)	2.60 (0.000)	12.20 (0.000)	-3.57 (0.131)	3.66 (0.087)	-6.90 (0.000)	6.50 (0.002)	-5.79 (0.004)
CF_Amyg	-0.08 (0.875)	-1.07 (0.023)	17.75 (0.000)	13.63 (0.000)	9.73 (0.000)	7.47 (0.000)	12.40 (0.000)	9.53 (0.000)
CF_AC	-2.17 (0.041)	1.93 (0.048)	-4.93 (0.017)	-1.31 (0.469)	-3.24 (0.003)	-2.31 (0.019)	-3.81 (0.002)	-1.98 (0.055)
CF_PC	3.17 (0.000)	1.05 (0.004)	25.86 (0.000)	20.60 (0.000)	3.50 (0.000)	3.85 (0.000)	10.95 (0.000)	9.44 (0.000)

SF7. The β_1 and P values of WMHL derived from the linear model at five levels of tract grouping

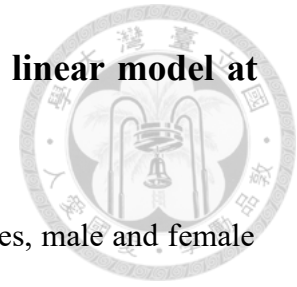
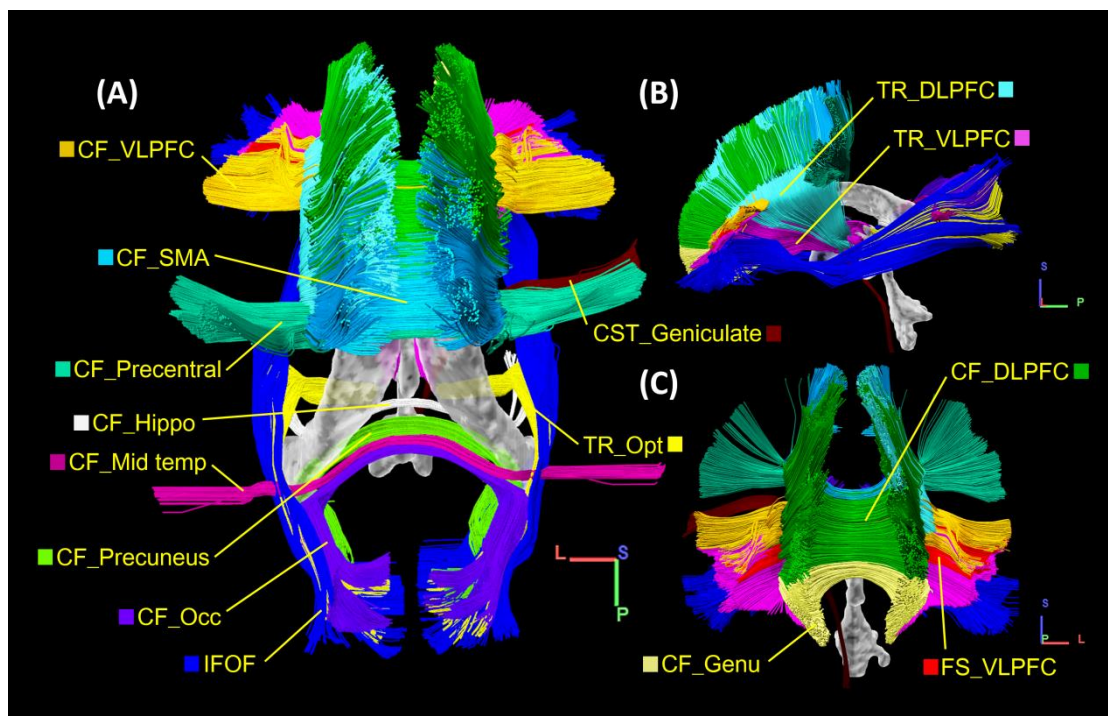


Table SF7. The rate of change in WMHL in terms of β_1 and P values, male and female participants listed separately. The left column of the table lists β_1 and P values in the whole brain, three fiber systems, ten subsystems, and 25 tract groups. The middle and right columns list the values in the 76 tracts.

Tract	WMHL		Tract	WMHL		Tract	WMHL	
	β_1 (P-Value)	F		β_1 (P-Value)	F		β_1 (P-Value)	F
Whole brain	0.024 (0.000)	0.025 (0.000)	76 tracts					
3 systems			L CGB	-0.023 (0.002)	-0.011 (0.072)	L FS_OFC	0.010 (0.000)	0.023 (0.001)
Association	0.003 (0.025)	0.006 (0.002)	R CGB	-0.020 (0.003)	-0.010 (0.138)	R FS_OFC	0.020 (0.007)	0.019 (0.000)
Projection	0.016 (0.000)	0.023 (0.000)	L CGH	0.000 (0.498)	0.000 (0.869)	L FS_VLPFC	0.148 (0.000)	0.186 (0.000)
Commissure	0.075 (0.000)	0.069 (0.000)	R CGH	0.002 (0.152)	0.000 (0.931)	R FS_VLPFC	0.127 (0.000)	0.154 (0.000)
10 subsystems			L FX	0.025 (0.066)	0.006 (0.000)	L FS_DLPFC	0.019 (0.002)	0.012 (0.000)
limbic	-0.003 (0.264)	0.002 (0.481)	R FX	0.000 (0.961)	0.009 (0.128)	R FS_DLPFC	0.007 (0.000)	0.004 (0.296)
Cortical-Cortical	0.009 (0.000)	0.010 (0.001)	L ST	-0.009 (0.494)	-0.005 (0.892)	L FS_Mot	0.016 (0.011)	0.031 (0.001)
Sensorimotor	0.003 (0.001)	0.015 (0.007)	R ST	-0.002 (0.884)	0.039 (0.001)	R FS_Mot	0.034 (0.016)	0.073 (0.000)
FS	0.034 (0.000)	0.047 (0.000)	L UF	0.002 (0.605)	0.012 (0.009)	L TR_VLPFC	0.017 (0.000)	0.023 (0.000)
TR	0.027 (0.000)	0.023 (0.000)	R UF	0.015 (0.000)	0.004 (0.463)	R TR_VLPFC	0.021 (0.000)	0.019 (0.000)
CF_Front	0.047 (0.000)	0.052 (0.000)	L AF	0.021 (0.005)	0.031 (0.002)	L TR_DLPFC	0.007 (0.000)	0.006 (0.000)
CF_Par	0.090 (0.000)	0.064 (0.000)	R AF	0.033 (0.000)	0.031 (0.007)	R TR_DLPFC	0.008 (0.000)	0.006 (0.000)
CF_Occ	0.043 (0.000)	0.045 (0.000)	L FAT	0.016 (0.001)	0.024 (0.003)	L TR_Precentral	0.064 (0.000)	0.088 (0.002)
CF_Temp	0.171 (0.000)	0.158 (0.000)	R FAT	0.034 (0.001)	0.015 (0.005)	R TR_Precentral	0.015 (0.000)	0.034 (0.002)
CF_Comm	0.002 (0.001)	0.000 (0.540)	L IFOF	0.029 (0.000)	0.031 (0.000)	L TR_Postcentral	0.018 (0.001)	0.006 (0.373)
25 tract groups			R IFOF	0.024 (0.000)	0.025 (0.000)	R TR_Postcentral	0.019 (0.028)	0.016 (0.030)
CGB	-0.017 (0.000)	-0.010 (0.028)	L ILF	-0.001 (0.564)	-0.001 (0.535)	L TR_Aud	-0.003 (0.137)	-0.001 (0.205)
CGH	0.001 (0.108)	0.000 (0.943)	R ILF	0.002 (0.046)	0.004 (0.071)	R TR_Aud	0.000 (0.384)	0.000 (0.803)
FX	0.010 (0.209)	0.007 (0.013)	L PF	0.034 (0.003)	0.041 (0.060)	L TR_Opt	0.143 (0.000)	0.120 (0.000)
ST	-0.008 (0.397)	0.017 (0.337)	R PF	0.022 (0.002)	0.030 (0.031)	R TR_Opt	0.146 (0.000)	0.106 (0.000)
UF	0.006 (0.014)	0.007 (0.039)	L SLF I	0.003 (0.040)	0.005 (0.021)	CF_Genu	0.030 (0.000)	0.041 (0.000)
AF	0.022 (0.000)	0.027 (0.000)	R SLF I	0.002 (0.478)	0.005 (0.098)	CF_DLPFC	0.004 (0.000)	0.005 (0.000)
FAT	0.021 (0.000)	0.017 (0.000)	L SLF II	0.011 (0.093)	0.013 (0.142)	CF_VLPFC	0.137 (0.000)	0.144 (0.000)
IFOF	0.023 (0.000)	0.025 (0.000)	R SLF II	0.010 (0.025)	0.003 (0.538)	CF_SMA	0.012 (0.000)	0.011 (0.000)
ILF	0.000 (0.527)	0.002 (0.232)	L SLF III	0.010 (0.063)	0.011 (0.256)	CF_Precentral	0.084 (0.000)	0.088 (0.000)
PF	0.024 (0.001)	0.029 (0.026)	R SLF III	0.003 (0.535)	0.017 (0.136)	CF_Postcentral	0.025 (0.083)	0.020 (0.018)
SLF	0.004 (0.049)	0.007 (0.099)	L CST_Toe	-0.002 (0.191)	0.001 (0.694)	CF_Paracentral	0.036 (0.000)	0.038 (0.000)
CST	0.004 (0.001)	0.018 (0.006)	R CST_Toe	0.001 (0.002)	0.000 (0.585)	CF_SPL	0.350 (0.002)	0.238 (0.005)
ML	0.000 (0.230)	0.000 (0.886)	L CST_Trunk	-0.002 (0.343)	0.001 (0.462)	CF_IPL	0.040 (0.001)	0.032 (0.001)
FS_Pfc	0.044 (0.000)	0.055 (0.000)	R CST_Trunk	0.003 (0.000)	0.010 (0.028)	CF_Precuneus	0.099 (0.000)	0.067 (0.000)
FS_Mot	0.020 (0.006)	0.045 (0.000)	L CST_Hand	0.013 (0.001)	0.077 (0.113)	CF_Occ	0.043 (0.000)	0.045 (0.000)
TR_Pfc	0.011 (0.000)	0.011 (0.000)	R CST_Hand	0.001 (0.053)	0.017 (0.189)	CF_Sup Temp	0.033 (0.001)	0.027 (0.001)
TR_Sm	0.023 (0.000)	0.031 (0.002)	L CST_Mouth	0.007 (0.136)	0.018 (0.013)	CF_Mid Temp	0.845 (0.000)	0.707 (0.000)
TR_Aud	-0.002 (0.155)	-0.001 (0.213)	R CST_Mouth	0.027 (0.003)	0.051 (0.005)	CF_Temp Pole	0.007 (0.532)	0.030 (0.024)
TR_Opt	0.135 (0.000)	0.100 (0.000)	L CST_Geniculate	0.005 (0.154)	0.017 (0.001)	CF_Hippo	0.098 (0.000)	0.177 (0.000)
CF_Pfc	0.043 (0.000)	0.047 (0.000)	R CST_Geniculate	0.012 (0.000)	0.024 (0.000)	CF_Amyg	0.033 (0.324)	0.057 (0.004)
CF_Sm	0.042 (0.000)	0.044 (0.000)	L ML	0.000 NaN	0.000 (0.562)	CF_AC	0.004 (0.001)	-0.001 (0.284)
CF_Par	0.136 (0.001)	0.097 (0.001)	R ML	0.001 (0.230)	0.000 (0.618)	CF_PC	0.000 (0.969)	0.000 (0.189)
CF_Occ	0.043 (0.000)	0.045 (0.000)						
CF_Temp	0.171 (0.000)	0.158 (0.000)						
CF_Comm	0.002 (0.001)	0.000 (0.540)						

Figure SF7. The tracts that showed highest rates of WMHL increase, viewed from top (A), from side (B) and from front (C). Note that these tracts form a cluster surrounding the lateral ventricles, corresponding to the typical WMHL locations in the periventricular white matter.



The cluster comprised 19 tracts occupying the periventricular white matter of the lateral ventricles. To assess whether these 19 tracts also had higher WMHL loads than the rest of the 57 tracts, the means of WMHL of the 19 tracts and that of the 57 tracts were compared using the two-sample t-test. Significant differences were found in both male (0.4013 ± 0.46806 vs. 0.0371 ± 0.04244 , $p = 0.000$) and female (0.3395 ± 0.34107 vs. 0.0432 ± 0.04801) participants.

SF8. Normative models of white matter tract integrity of the UK Biobank cohort



Table SF8 lists the mean values of GFA, AD, RD, MD, and WMHL of the whole white matter tracts at each year. At 47 years of age the mean GFA, AD, RD, MD and WMHL values were 0.465, 1.030 (10^{-3} mm²/s), 0.443 (10^{-3} mm²/s), 0.638 (10^{-3} mm²/s) and 0.224%, respectively, whereas at 76 years the values were 0.460, 1.055 (10^{-3} mm²/s), 0.455 (10^{-3} mm²/s), 0.655 (10^{-3} mm²/s) and 0.589%, respectively.

Table SF8. The mean values of GFA, AD, RD, MD, and WMHL of the whole white matter tracts at each year.

Age	GFA			AD*10 ⁻³ mm ² /Sec			RD*10 ⁻³ mm ² /Sec			MD*10 ⁻³ mm ² /Sec			WMHL(%)		
	All	M	F	All	M	F	All	M	F	All	M	F	All	M	F
47	0.465 (0.065)	0.466 (0.065)	0.464 (0.065)	1.030 (0.100)	1.030 (0.100)	1.029 (0.100)	0.443 (0.053)	0.441 (0.053)	0.444 (0.052)	0.638 (0.042)	0.638 (0.043)	0.639 (0.042)	0.224	0.325	0.048
48	0.466 (0.065)	0.467 (0.065)	0.465 (0.066)	1.028 (0.098)	1.025 (0.098)	1.030 (0.099)	0.442 (0.055)	0.440 (0.054)	0.443 (0.055)	0.637 (0.044)	0.635 (0.044)	0.639 (0.044)	0.193	0.165	0.209
49	0.466 (0.065)	0.466 (0.065)	0.467 (0.065)	1.027 (0.099)	1.028 (0.099)	1.026 (0.099)	0.440 (0.055)	0.440 (0.055)	0.440 (0.055)	0.636 (0.044)	0.636 (0.044)	0.635 (0.045)	0.081	0.059	0.097
50	0.466 (0.065)	0.466 (0.065)	0.465 (0.065)	1.028 (0.099)	1.027 (0.099)	1.029 (0.098)	0.442 (0.055)	0.441 (0.055)	0.443 (0.055)	0.637 (0.045)	0.636 (0.044)	0.638 (0.045)	0.205	0.287	0.085
51	0.466 (0.065)	0.468 (0.065)	0.464 (0.066)	1.027 (0.100)	1.025 (0.100)	1.029 (0.100)	0.441 (0.055)	0.437 (0.055)	0.445 (0.055)	0.636 (0.044)	0.633 (0.044)	0.639 (0.044)	0.112	0.118	0.107
52	0.466 (0.065)	0.468 (0.066)	0.464 (0.065)	1.028 (0.099)	1.029 (0.101)	1.027 (0.098)	0.440 (0.055)	0.438 (0.056)	0.442 (0.054)	0.636 (0.044)	0.635 (0.045)	0.637 (0.043)	0.114	0.102	0.124
53	0.466 (0.065)	0.467 (0.065)	0.466 (0.065)	1.026 (0.098)	1.025 (0.100)	1.027 (0.097)	0.439 (0.055)	0.438 (0.055)	0.440 (0.055)	0.635 (0.044)	0.634 (0.044)	0.636 (0.044)	0.086	0.084	0.087
54	0.465 (0.066)	0.468 (0.066)	0.464 (0.066)	1.028 (0.099)	1.026 (0.099)	1.029 (0.098)	0.441 (0.055)	0.438 (0.055)	0.443 (0.055)	0.637 (0.044)	0.634 (0.044)	0.639 (0.044)	0.145	0.050	0.184
55	0.466 (0.065)	0.469 (0.065)	0.464 (0.065)	1.023 (0.098)	1.023 (0.098)	1.023 (0.098)	0.439 (0.055)	0.436 (0.055)	0.441 (0.055)	0.633 (0.044)	0.632 (0.044)	0.635 (0.045)	0.082	0.084	0.081
56	0.464 (0.065)	0.468 (0.065)	0.462 (0.065)	1.026 (0.098)	1.024 (0.099)	1.027 (0.098)	0.441 (0.055)	0.437 (0.056)	0.444 (0.055)	0.636 (0.044)	0.633 (0.045)	0.638 (0.044)	0.104	0.109	0.101
57	0.465 (0.066)	0.466 (0.066)	0.463 (0.065)	1.029 (0.098)	1.028 (0.100)	1.029 (0.097)	0.442 (0.056)	0.440 (0.058)	0.444 (0.056)	0.638 (0.045)	0.636 (0.046)	0.639 (0.044)	0.112	0.103	0.117
58	0.465 (0.065)	0.468 (0.065)	0.464 (0.065)	1.028 (0.099)	1.026 (0.101)	1.030 (0.098)	0.441 (0.056)	0.437 (0.056)	0.444 (0.056)	0.637 (0.045)	0.634 (0.046)	0.639 (0.045)	0.112	0.122	0.102
59	0.464 (0.065)	0.465 (0.065)	0.463 (0.065)	1.030 (0.098)	1.030 (0.100)	1.031 (0.096)	0.443 (0.056)	0.442 (0.056)	0.445 (0.056)	0.639 (0.044)	0.638 (0.045)	0.640 (0.044)	0.196	0.142	0.225
60	0.464 (0.066)	0.467 (0.065)	0.462 (0.066)	1.029 (0.098)	1.027 (0.099)	1.030 (0.097)	0.443 (0.056)	0.439 (0.056)	0.446 (0.056)	0.638 (0.044)	0.635 (0.045)	0.640 (0.044)	0.149	0.147	0.151
61	0.463 (0.065)	0.466 (0.066)	0.460 (0.064)	1.031 (0.097)	1.033 (0.099)	1.030 (0.096)	0.445 (0.055)	0.442 (0.056)	0.447 (0.055)	0.640 (0.043)	0.639 (0.044)	0.642 (0.043)	0.171	0.176	0.166
62	0.464 (0.065)	0.465 (0.065)	0.463 (0.065)	1.031 (0.097)	1.031 (0.099)	1.030 (0.096)	0.443 (0.057)	0.442 (0.057)	0.445 (0.057)	0.639 (0.045)	0.638 (0.045)	0.640 (0.045)	0.210	0.233	0.193
63	0.463 (0.065)	0.465 (0.065)	0.461 (0.065)	1.033 (0.097)	1.031 (0.098)	1.034 (0.096)	0.445 (0.058)	0.442 (0.059)	0.448 (0.057)	0.641 (0.045)	0.639 (0.047)	0.643 (0.044)	0.247	0.236	0.255
64	0.462 (0.065)	0.463 (0.065)	0.461 (0.065)	1.034 (0.097)	1.036 (0.099)	1.033 (0.096)	0.447 (0.058)	0.446 (0.058)	0.448 (0.057)	0.643 (0.045)	0.642 (0.047)	0.643 (0.045)	0.303	0.335	0.274
65	0.464 (0.065)	0.466 (0.065)	0.461 (0.065)	1.032 (0.097)	1.033 (0.099)	1.031 (0.097)	0.444 (0.058)	0.441 (0.058)	0.447 (0.058)	0.640 (0.045)	0.638 (0.046)	0.642 (0.045)	0.271	0.277	0.265
66	0.464 (0.066)	0.466 (0.066)	0.462 (0.065)	1.034 (0.097)	1.037 (0.098)	1.032 (0.096)	0.444 (0.058)	0.443 (0.058)	0.446 (0.057)	0.641 (0.044)	0.641 (0.045)	0.641 (0.044)	0.360	0.331	0.387
67	0.462 (0.066)	0.465 (0.066)	0.460 (0.065)	1.038 (0.097)	1.037 (0.099)	1.039 (0.096)	0.447 (0.059)	0.444 (0.060)	0.450 (0.058)	0.644 (0.046)	0.641 (0.047)	0.646 (0.045)	0.313	0.289	0.334
68	0.461 (0.065)	0.464 (0.065)	0.459 (0.065)	1.036 (0.097)	1.038 (0.099)	1.035 (0.096)	0.447 (0.059)	0.445 (0.059)	0.450 (0.058)	0.644 (0.046)	0.643 (0.047)	0.645 (0.045)	0.387	0.302	0.458
69	0.461 (0.065)	0.465 (0.065)	0.457 (0.065)	1.037 (0.097)	1.037 (0.099)	1.038 (0.095)	0.448 (0.059)	0.444 (0.060)	0.452 (0.059)	0.644 (0.046)	0.641 (0.048)	0.647 (0.045)	0.392	0.366	0.418
70	0.462 (0.065)	0.464 (0.066)	0.460 (0.065)	1.041 (0.097)	1.043 (0.100)	1.039 (0.095)	0.448 (0.060)	0.446 (0.061)	0.450 (0.059)	0.646 (0.046)	0.645 (0.048)	0.646 (0.045)	0.378	0.398	0.356
71	0.463 (0.065)	0.467 (0.065)	0.458 (0.065)	1.043 (0.096)	1.045 (0.098)	1.041 (0.095)	0.447 (0.060)	0.444 (0.060)	0.452 (0.060)	0.646 (0.046)	0.644 (0.047)	0.648 (0.046)	0.409	0.369	0.456
72	0.462 (0.066)	0.464 (0.066)	0.458 (0.065)	1.044 (0.098)	1.045 (0.101)	1.043 (0.095)	0.450 (0.061)	0.446 (0.061)	0.454 (0.061)	0.648 (0.048)	0.646 (0.049)	0.650 (0.047)	0.570	0.417	0.712
73	0.462 (0.065)	0.465 (0.065)	0.458 (0.064)	1.042 (0.097)	1.043 (0.099)	1.042 (0.095)	0.448 (0.061)	0.445 (0.061)	0.453 (0.060)	0.646 (0.048)	0.645 (0.049)	0.649 (0.047)	0.336	0.281	0.411
74	0.462 (0.065)	0.465 (0.065)	0.458 (0.065)	1.044 (0.096)	1.045 (0.098)	1.043 (0.094)	0.450 (0.061)	0.447 (0.061)	0.452 (0.060)	0.648 (0.047)	0.647 (0.049)	0.649 (0.046)	0.497	0.424	0.574
75	0.465 (0.065)	0.467 (0.065)	0.461 (0.066)	1.046 (0.099)	1.045 (0.100)	1.047 (0.098)	0.446 (0.062)	0.442 (0.063)	0.452 (0.061)	0.646 (0.049)	0.643 (0.050)	0.650 (0.047)	0.441	0.439	0.443
76	0.460 (0.065)	0.462 (0.065)	0.457 (0.065)	1.055 (0.098)	1.059 (0.100)	1.050 (0.096)	0.455 (0.062)	0.454 (0.062)	0.457 (0.061)	0.655 (0.049)	0.655 (0.050)	0.655 (0.047)	0.589	0.503	0.704

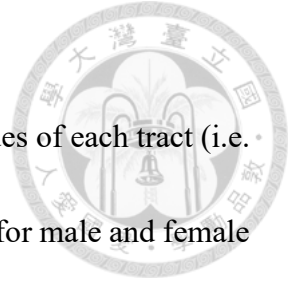


Figure SF8. Plots of means and standard deviations of the index values of each tract (i.e. GFA, AD, RD, MD and WMHL) at each year of age, in blue and red for male and female participants, respectively. The stick at each year represents the width of 2 standard deviations centered at the mean value. The solid lines spanned from 47 to 76 years were rendered according to the slopes and intercepts of each tract calculated from the linear regression model.

